Atmospheric teleconnection processes linking winter air stagnation and haze extremes in China with regional Arctic sea ice decline

Yufei Zou[1], Yuhang Wang[2], Zuowei Xie[3], Hailong Wang[1], Philip J. Rasch[1]

[1]Atmospheric Sciences and Global Change Division, Pacific Northwest National Laboratory, Richland, WA 99354, USA
[2]School of Earth and Atmospheric Sciences, Georgia Institute of Technology, Atlanta, GA 30332, USA
[3]International Center for Climate and Environment Sciences, Institute of Atmospheric Physics, Chinese Academy of Sciences, Beijing, 100029, China

Correspondence: Yufei Zou (yufei.zou@pnnl.gov) and Yuhang Wang (yuhang.wang@eas.gatech.edu)

Abstract. Recent studies suggested significant impacts of boreal cryosphere changes on wintertime air stagnation and haze pollution extremes in China. However, the underlying mechanism of such a teleconnection relationship remains unclear. Here we used the Whole Atmosphere Community Climate Model (WACCM) to investigate dynamic processes leading to atmospheric circulation and air stagnation responses to Arctic sea ice changes. We conducted four climate sensitivity experiments by perturbing sea ice concentrations (SIC) and corresponding sea surface temperature (SST) in autumn and early winter over the whole Arctic and three sub-regions in the climate model. The results indicate different responses in the general circulation and regional ventilation to the region-specific Arctic changes, with the largest increase of both the probability (by 120%) and the intensity (by 32%) of air stagnation extreme events being found in the experiment driven by SIC and SST changes over the Pacific sector of the Arctic (the East Siberian and Chukchi Seas). The increased air stagnation extreme events are mainly driven by an amplified hemispheric-scale atmospheric teleconnection pattern that resembles the negative phase of the Eurasian (EU) pattern. Dynamical diagnostics suggest that convergence of transient eddy forcing in the vicinity of Scandinavia in winter is largely responsible for the amplification of the teleconnection pattern. Transient eddy vorticity fluxes dominate the transient eddy forcing and produce a barotropic anticyclonic anomaly near Scandinavia and wave-train propagation across Eurasia to the downstream regions in East Asia. The piecewise potential vorticity inversion analysis reveals that this long-range atmospheric teleconnection of the Arctic origin takes place primarily in the middle and upper troposphere. The anomalous ridge over East Asia in the middle and upper troposphere worsens regional ventilation conditions by weakening monsoon northwesterlies and enhancing temperature inversion near the surface, leading to more and stronger air stagnation and pollution extremes over eastern China in winter. Ensemble projections based on the state-of-the-art climate models in the Coupled Model Intercomparison Project Phase 6 (CMIP6) corroborate this teleconnection relationship between high-latitude environmental changes and middle-latitude weather extremes, though the tendency and magnitude vary considerably among each participating model.

1 Introduction

The severe haze pollution over the East China Plains (ECP) in recent boreal winter has drawn broad attention because of its profound public health (Kan et al., 2012), socioeconomic (Xie et al., 2016), and climatic impacts (Li et al., 2016). In response to these environmental stressors, the Chinese government has prioritized environment protection to address the urgent public health needs (State Council of China, 2013). Many studies have investigated from various perspectives the possible causes of the severe haze pollution, ranging from massive primary emissions (Liu et al., 2016; Sun et al., 2016), rapid secondary pollution formation (Cheng et al., 2016; Huang et al., 2014; Guo et al., 2014; Wang et al., 2016), unfavorable regional circulation features (Jia et al., 2015; Niu et al., 2010; Yin and Wang, 2017), and positive aerosol-weather feedback effects (Zhang et al., 2018; Zhong et al., 2018; Lou et al., 2019). An et al. (2019) provides a recent review of the severe haze problems in China and emphasized the synergistic effect of all these contributing features. It has also been reported that climate change plays an important role in generating conducive meteorological conditions for the favorable formation and unfavorable ventilation for air pollution in China and many other regions (Cai et al., 2017; Dawson et al., 2014; Horton et al., 2014; Wang and Chen, 2016). Several possible climate factors have been investigated for their effects on winter haze pollution in China, including: 1) Arctic sea ice (Wang et al., 2015; Zou et al., 2017); 2) Eurasian snow cover (Yin and Wang, 2018; Zou et al., 2017); 3) El Niño–Southern Oscillation (ENSO; Chang et al., 2016; Sun et al., 2018; Zhao et al., 2018; Zhang et al., 2019); 4) Pacific Decadal Oscillation (PDO; Zhao et al., 2016); and 5) the northwestern Pacific sea surface temperature (SST; Pei et al., 2018). In these studies, researchers mainly focused on the relationships of various climate factors with pollution-related weather conditions such as the intensity of East Asia winter monsoon (EAWM), planetary boundary layer height, precipitation, and circulation patterns that correlated with winter haze pollution in China. The data analysis results were further corroborated by modeling studies (Zhao et al., 2016; Zhao et al., 2018; Zhang et al., 2019; Zou et al., 2017). However, a clear understanding of key dynamic processes linking complex meteorological changes to critical climate factors was still missing, which is necessary to establish a robust causal relationship between remote climate drivers and local atmospheric responses because a good correlation does not necessarily imply causation. Other studies have examined future projections of future air stagnation conditions based on the Coupled Model Intercomparison Project Phase 5 (CMIP5) high emission scenario (RCP8.5) data (Taylor et al., 2012) and ended up with contradictory conclusions over the eastern China region (Cai et al., 2017; Horton et al., 2014), which further highlights the importance of physical process-based analysis of modeling results. Given the increasing evidence of the profound influence of climate change—especially that occurring in high-latitude regions—on middle-latitude circulation and weather extremes (Cohen et al., 2014; IPCC, 2019), it is imperative to identify the key atmospheric processes driving the circulation responses and to understand the underlying physical mechanisms. Therefore, here we have re-analyzed the particular linkage between Arctic sea ice change and wintertime air stagnation in China identified by our previous study (Zou et al., 2017) and elucidated the teleconnection mechanism based on new climate model sensitivity experiments and dynamic diagnoses. We describe the analytical methods and datasets in Sect. 2 and analysis of model results in Sect. 3, which is followed by discussion and conclusions in Sect. 4.

2 Analysis methods and datasets

2.1 Observation and reanalysis data

We collected monthly gridded Arctic sea ice concentration (SIC) and sea surface temperature (SST) data for 1950-2018 from the Met Office Hadley Centre (HadISST; Rayner et al., 2003) for statistical
5 analysis and comparison to numerical simulation experiments. We conducted trend analysis for Arctic sea ice changes and investigated the statistical correlation between these changes and key atmospheric circulation patterns of interest. The National Centers for Environmental Prediction and National Center of Atmospheric Research (NCEP/NCAR) reanalysis data (Kalnay et al., 1996) was used to calculate indices of a hemispheric-scale Eurasian (EU) pattern (Wallace and Gutzler, 1981) and a regional
10 circulation pattern (MCA_Z500) over East Asia in the 500 hPa geopotential height field (Z500) (Fig. S1 in the Supplement). The latter pattern was determined using a Maximum Covariance Analysis (MCA) method (Wilks, 2011) as in our previous study (Zou et al., 2017). We focused on these two circulation patterns at different spatial scales given their considerable impacts on winter synoptic weather (Liu et al., 2014; Wang and Zhang, 2015) and regional haze pollution (Li et al., 2019) in China. We also used
15 the NCEP/NCAR reanalysis data to calculate a pollution potential index (PPI) as a synthetic meteorological proxy for describing regional air stagnation severity (Zou et al., 2017). We followed the definition of the EU index (EUI) in Wallace and Gutzler (1981) and calculated the EU index in winter (December-January-February; DJF) from 1951 to 2019 (years are aligned with January of the winter season in this work),

$$EUI = -\frac{1}{4}Z^*(55° N, 20° E) + \frac{1}{2}Z^*(55° N, 75° E) - \frac{1}{4}Z^*(40° N, 145° E) \quad , \quad (1)$$

where Z^* denotes the normalized monthly mean geopotential height anomalies at 500 hPa using the 1981-2010 average as the climatology. We then regressed the 500 hPa geopotential height anomalies onto this index to get the EU spatial pattern (Fig. 1), which resembles those reported in Liu et al. (2014); Wallace and Gutzler, (1981) and Wang and Zhang (2015) quite well.
25 We then calculated winter (DJF) PPI in 1951-2019 based on normalized surface wind speed and near surface temperature gradient of the reanalysis data in Eq. (2). We first standardized surface wind speed and potential temperature gradient between 925 hPa and 1000 hPa for each grid cell by subtracting their time-averaged values over 1981-2010 and dividing by the standard deviations in the same period. We then estimated grid-scale PPI by weighted averaging wind speed index (WSI) and air temperature
30 gradient index (ATGI),

$$PPI = \frac{r_1 \times WSI + r_2 \times ATGI}{|r_1| + |r_2|} \quad , \quad (2)$$

where r_1 and r_2 are the Person correlation coefficients of WSI (r_1 = -0.73) and ATGI (r_2 = 0.70) with in situ PM_{10} observations over the ECP area (Zou et al., 2017). The regional averaged ECP_PPI was estimated by averaging grid-scale PPI over the ECP area (112° E to 122° E, 30° N to 41° N).
35 Lastly, we applied the MCA method to the Z500 and PPI fields and identified the regional MCA_Z500 pattern that had the largest covariance with PPI changes in ECP. The MCA analysis performs a singular value decomposition of the covariance matrix of the selected two variables and generates a series of coupled modes in space and time dimensions for both variables (Wilks, 2011). We chose the first couple of modes in the Z500 and PPI fields as the MCA_Z500 and MCA_PPI patterns

that show the largest covariance with each other (r=0.65; Fig. S1 in the Supplement). The MCA_Z500 pattern resembles a regional manifestation of the hemispheric-scale EU pattern (in negative phase) with a good correlation between these two indices (r=-0.67; Fig. S1 in the Supplement). However, it's worth noting that this regional MCA_Z500 pattern can also be excited by other large-scale teleconnection

5 processes associated with both natural variability and perturbed atmospheric wave activity. These variables were assessed as metrics of circulation and ventilation responses to climate forcing in the following sections.

2.2 Climate models and numerical sensitivity experiments

This study uses the high-top Whole Atmosphere Community Climate Model (WACCM) version 5

10 (Marsh et al., 2013) under the common numerical framework of the NCAR Community Earth System Model (CESM) for climate sensitivity experiments. WACCM is a comprehensive atmospheric model with a well-resolved stratosphere of 70 vertical layers spanning the surface to the thermosphere (~0.001 hPa) at a horizontal resolution of 1.9° (latitude) ×2.5° (longitude). We conducted 30-year simulations (with an additional unanalyzed 1-year period for the control run as spin-up) as the control (CTRL) run

15 with annually repeating prescribed climatological (1981-2010 average) Arctic SIC and SST from the Met Office Hadley Centre (Rayner et al., 2003) (Table 1). We then performed four climate sensitivity experiments by perturbing SIC and SST in different Arctic regions to investigate the climate sensitivity to regional Arctic sea ice changes and associated local ocean warming (Screen et al., 2013). The spatial distribution of correlation coefficients between SIC and EU indices (Fig. 1b) indicated varying climate

20 sensitivity relationships between regional sea ice changes and circulation responses as suggested by previous studies (Screen, 2017; Sun et al., 2015; McKenna et al., 2018). To test this region-specific climate sensitivity, we first perturbed SIC and SST in the whole Arctic region to evaluate their comprehensive climate effects, and then divided the whole Arctic region into three sub-regions (R1-R3; Fig. 1b) and perturbed regional SIC and SST in three region-specific numerical experiments (Table 1).

25 Specifically, we branched an 8-month simulation from each July of the CTRL run with observed SIC/SST data in autumn and early winter (August-November) of 2012 over the whole Arctic in the first sensitivity experiment (SENSall). We chose 2012 because it has the lowest level of Arctic sea ice concentrations throughout the satellite era of the last four decades (NSIDC/NASA, 2019) and provides the strongest sea-ice perturbation to the climate system. We only changed the surface boundary

30 conditions (SIC/SST) at these modeling grid cells with SIC anomalies larger than 10% to focus on the Arctic regions with the most significant changes. We then added three region-specific sensitivity experiments (SENSr1/r2/r3) by perturbing regional SIC and SST in R1-R3 regions (R1: 30° E to 150° E, 70° N to 85° N; R2: 150° E to 145° W, 60° N to 85° N; R3: 145° W to 30° W, 50° N to 85° N; Fig. 1b) respectively following the same perturbation method in SENSall. We analyzed the continuous

35 December-January-February data at the end of each sensitivity simulation to examine the seasonal impact of Arctic sea ice changes in comparison with observation and reanalysis data. The simulated EU/MCA_Z500 circulation indices were estimated by projecting modeling differences (SENSx-CTRL, x=all/r1/r2/r3) onto the reanalysis-based EU/MCA_Z500 patterns, and the ECP_PPI indices in the model were calculated following the same method of the reanalysis one by using the CTRL ensemble

40 mean as the climatology.

Since the default 2000-based emission inventory (Lamarque et al., 2010) in WACCM was prepared for the Fifth Assessment Report of the Intergovernmental Panel on Climate Change (IPCC AR5) and is low biased over China, we updated the anthropogenic emission inventory in China by replacing the default one with the 2010-based multi-resolution emission inventory for China (MEIC; Li et al., 2017).

5   The MEIC-MIX inventory was developed for the years 2008 and 2010 and has been widely used for air pollution simulation and health impact assessment studies in China (Geng et al., 2017; Zhang et al., 2017). It is worth noting that the main objective of this study is not to reproduce severe haze pollution extremes in China, but to understand how regional atmosphere and pollution conditions respond to the key climate drivers in the high latitudes. Therefore, we only focused on the relative changes of PPI and

10   surface $PM_{2.5}$ concentrations between SENS and CTRL experiments and investigated dynamic processes associated with these changes in our following analysis.

Besides the CESM-WACCM model used in the sensitivity experiments, we also analyzed modeling results from other state-of-the-art climate models in the latest CMIP6 project to examine the teleconnection relationship between Arctic sea ice and regional air stagnation in China. Table S1 in the

15   Supplement lists the 8 CMIP6 models with the same experiment and variant ID (r1i1p1f1) used for historical simulations and future projections of the Arctic sea ice extent (SIE) and ECP_PPI time series. SIE is a measurement of the ocean area where sea ice concentrations exceed 15% (NSIDC, 2019). We analyzed historical simulations (1950-2014; Eying et al., 2016) and future projections (2015-2100) of the Shared Socioeconomic Pathway under a high greenhouse gas emission scenario (SSP5-8.5; O'Neill

20   et al., 2016) by each model to maintain consistency with previous studies (Cai et al., 2017; Horton et al., 2014). We then calculated time series of regional averaged Arctic SIE and ECP_PPI in each CMIP6 model to estimate ensemble means and standard deviations of these variables. The estimation of the SIE relative changes and ECP_PPI indices in CMIP6 followed the same method of the observation- and reanalysis-based ones by using 1981-2010 historical runs as the climatology. The whole CMIP6 time

25   series of the 150 years were equally divided into three time periods (P1-P3) to evaluate regional air stagnation conditions under different Arctic sea ice forcing.

2.3 Statistical analysis methods

We examined long-term linear trends of observed SIC in each grid cell in Fig. 1 using the Mann-Kendall test, which is a non-parametric (i.e., distribution free) method that is based on the relative

30   ranking of data values. After trend detection, we estimated the Pearson correlation between the gridded sea ice variations and the EU index. To evaluate the circulation impact on regional ventilation, we conducted composite analysis of gridded PPIs over the middle latitude regions and examined their statistical significance using the two-sided Student's t-test. The t-test was also used to evaluate statistical significance of surface heat flux changes and atmospheric responses in the modeling results,

35   such as the ensemble mean differences of atmospheric variables between the WACCM SENS and CTRL experiments.

To further evaluate climate sensitivity modeling results, we used statistical functions in Python (https://docs.scipy.org/doc/scipy/reference/stats.html) to evaluate statistical properties of the modeling samples and estimate their cumulative distribution functions (CDFs) and probability density functions

40   (PDFs) following proper distributions. We first examined the statistics of the MCA_Z500 and ECP_PPI

indices in each experiment in terms of their location, scale, and shape (Table S2), and then conducted the Shapiro-Wilk normality test (Wilks, 2011) to examine whether the data conform to normal distributions (Fig. S2 and Fig. S3 in the Supplement). The null hypothesis of the normality test is that the sampling data from each experiment are drawn from a normal distribution. If the p-value is larger than 0.05, we failed to reject the null hypothesis and fitted normal distribution CDF/PDF curves to the data (30 years × 3 winter months = 90 samples). Otherwise, we rejected the null hypothesis and chose a proper non-Gaussian distribution to fit CDF/PDF curves to the data. Table S2 shows these statistical properties and test results of each experiment, which suggests that the data in most experiments conform to normal distributions except MCA_Z500 in SENSall and MCA_Z500/ECP_PPI in SENSr2. The statistics and histograms of the SENSall MCA_Z500 indices suggest a skew distribution to the left, while these of the SENSr2 MCA_Z500/ECP_PPI indices suggest a skew distribution to the right. Therefore, we fitted a left-skewed Gumbel distribution to the SENSall MCA_Z500 data and a right-skewed Gumbel distribution to the SENSr2 data, respectively. The goodness-of-fit results are shown in the Q-Q plots of Fig. S2 and Fig. S3 in the Supplement. After distribution fitting, we chose the 95th percentiles of the MCA_Z500 and ECP_PPI indices in CTRL as the thresholds of positive extremes and estimated the probability of extreme events in the four SENS experiments based on their fitted CDF curves (i.e., $P_{PPI_{SENS} \geq PPI_{CTRL}^{95th}}$). The average intensity of positive extreme values in each experiment was estimated by weighted averaging these values with their probabilities as weights. The fitted CDFs for all the WACCM experiments are shown in Fig. 3 and discussed below. For CMIP6 data, we used the same approach to fit CDF curves for each modeling and the reanalysis data in different time periods. The CDFs for three time periods over 1950-2000 (P1), 2001-2050 (P2), and 2051-2100 (P3) are shown in Fig. 7 and discussed later near that figure. The P1 time period over 1951-2000 was chosen as the reference period for the NCEP reanalysis and CMIP6 modeling data. The thresholds of positive extremes in the reanalysis and CMIP6 models were defined as the 95th percentiles of ECP_PPI values in this reference time period, which were then used to evaluate probability changes of extreme events in the other two periods (i.e., $P_{PPI_{P2/3} \geq PPI_{P1}^{95th}}$).

Such extreme value analyses provide an alternative perspective in addition to the traditional ensemble mean statistics with a more comprehensive understanding of atmospheric responses to climate forcing on full distribution curves. A special report of the Intergovernmental Panel on Climate Change (IPCC, 2012) focusing on the risks of climate extreme events proposed three kinds of responses including "shifted mean", "increased variability", and "changed symmetry" in climate variable distributions to climate change. These distinct responses demonstrate that changes in extremes can be linked to changes in the mean, variance, or shape of probability distributions, or all of these (IPCC, 2012). We followed this analysis framework to examine statistical distribution changes in regional circulation (MCA_Z500) and ventilation (ECP_PPI) with consideration of both natural variability and perturbation-induced responses in our climate sensitivity experiments. The uncertainty of the extreme probabilities and intensities in each experiment was evaluated using the bootstrap method by resampling the model simulated samples 5000 times and re-estimating those statistics based on the repeatedly fitted CDFs (Tables S3 and S4).

2.4 Diagnostics of atmospheric dynamics

To understand the atmospheric pathway from the Arctic sea ice forcing to regional circulation responses, we employed multiple dynamic diagnostic tools to investigate storm-track characteristics and local interactions between transient eddy forcing and the time-mean flow. The properties of transient
5 eddies were depicted by eddy kinetic energy (EKE) in Eq. (3) and the horizontal components of extended Eliassen-Palm vectors (**E** vectors) in Eq. (4) given by Hoskins et al. (1983),

$$EKE = \frac{1}{2}\left(\overline{u'^2} + \overline{v'^2}\right) \qquad , \qquad (3)$$

$$\boldsymbol{E}\ vector = \frac{1}{2}\left(\overline{v'^2} - \overline{u'^2}\right)\mathbf{i} - \overline{u'v'}\mathbf{j} \qquad , \qquad (4)$$

where u and v are the daily zonal and meridional wind components, respectively. The prime denotes the
10 2–8-day band-pass-filtered quantities and the overbar denotes time averaging over a month.
The direction of **E** vectors approximately points to the wave energy propagation relative to the local time-mean flow, while the divergence and curl of **E** vectors indicate eddy-induced acceleration of local mean zonal and meridional winds (Hoskins et al., 1983; Trenberth, 1986).
    We then illustrated transient eddy feedback to the quasi-stationary flow by eddy-induced
15 geopotential height tendencies due to the convergence and divergence of transient eddy vorticity and heat fluxes (Lau and Holopainen, 1984; Lau and Nath, 1991),

$$\left\{\frac{1}{f}\nabla^2 + f\frac{\partial}{\partial p}\left(\frac{1}{\sigma}\frac{\partial}{\partial p}\right)\right\}\left(\frac{\partial \phi}{\partial t}\right) = D^V + D^H, where\ D^V = -\nabla \cdot (\overline{V'\zeta'})\ and\ D^H = f\frac{\partial}{\partial p}\left(\frac{\nabla \cdot (\overline{V'\theta'})}{S}\right). \qquad (5)$$

    In Eq. (5), D^V and D^H are the eddy forcing due to heat and vorticity fluxes, respectively. f is the Coriolis parameter, $\phi = gz$ is geopotential, $\sigma = -\left(\frac{\alpha}{\theta}\right)\left(\frac{\partial \theta}{\partial p}\right)$ is static stability, α is specific volume, θ is
20 potential temperature with $S = -\frac{\partial \theta}{\partial p}$, V is horizontal wind, and ζ is relative vorticity. Here the prime and overbar are the same with these in Eqs. (3) and (4). By inverting the eddy forcing terms D^V and D^H on its right-hand side separately and solving the equation, we could distinguish each effect of vorticity and heat fluxes induced by transient eddies on the corresponding height tendencies Z_t^V and Z_t^H. The net tendency associated with the combination of D^V and D^H is denoted as Z_t^{V+H}.
25   Moreover, we used the phase-independent 3-dimensional wave activity flux (WAF; Takaya and Nakamura, 2001) based on the monthly averaged reanalysis and modeling data to diagnose zonal and vertical propagation of locally forced wave packet induced by quasi-geostrophic (QG) eddy disturbances embedded in a zonally varying basic flow,

$$\mathbf{W} = \frac{p\,cos\emptyset}{2|\mathbf{U}|}\left[\begin{array}{l}\frac{u}{a^2cos^2\emptyset}\left[\left(\frac{\partial \psi'}{\partial \lambda}\right)^2 - \psi'\frac{\partial^2 \psi'}{\partial \lambda^2}\right] + \frac{v}{a^2cos\emptyset}\left[\frac{\partial \psi'}{\partial \lambda}\frac{\partial \psi'}{\partial \emptyset} - \psi'\frac{\partial^2 \psi'}{\partial \lambda \partial \emptyset}\right] \\ \frac{u}{a^2cos^2\emptyset}\left[\frac{\partial \psi'}{\partial \lambda}\frac{\partial \psi'}{\partial \emptyset} - \psi'\frac{\partial^2 \psi'}{\partial \lambda \partial \emptyset}\right] + \frac{v}{a^2}\left[\left(\frac{\partial \psi'}{\partial \emptyset}\right)^2 - \psi'\frac{\partial^2 \psi'}{\partial \emptyset^2}\right] \\ \frac{f_0^2}{N^2}\left\{\frac{u}{a\,cos\emptyset}\left[\frac{\partial \psi'}{\partial \lambda}\frac{\partial \psi'}{\partial z} - \psi'\frac{\partial^2 \psi'}{\partial \lambda \partial z}\right] + \frac{v}{a}\left[\frac{\partial \psi'}{\partial \lambda}\frac{\partial \psi'}{\partial z} - \psi'\frac{\partial^2 \psi'}{\partial \lambda \partial z}\right]\right\}\end{array}\right] + \mathbf{C}_U M \qquad . \qquad (6)$$

30   Here $u\ and\ v$ are the zonal and meridional wind components, respectively. $\mathbf{U} = (u, v, 0)^T$ is a steady zonally inhomogeneous basic flow. $p = (\text{pressure}/1000\ \text{hPa})$ is normalized pressure, ψ' is a perturbation streamfunction, $(\emptyset, \lambda)$ are latitude and longitude, a is the earth's radius, $N^2 = (R_a p^\kappa/H)(\partial \theta/\partial z)$ is the squared buoyancy frequency, $\mathbf{C}_U$ represents the phase propagation in the

direction of **U**, and M can be interpreted as a generalization of small-amplitude pseudo-momentum for QG eddies onto a zonally varying basic flow.

Lastly, we quantified the influence of circulation anomalies at different vertical levels using a piecewise potential vorticity (PV) inversion method (Black and McDaniel, 2004). The PV anomalies
5   were calculated with reanalysis and simulation data for all troposphere pressure levels from 1000 hPa to 100 hPa in Eq. (7),

$$q' = \frac{1}{f}\left[\frac{1}{(a\cos\phi)^2}\frac{\partial^2}{\partial\lambda^2} + \frac{f}{a^2\cos\phi}\frac{\partial}{\partial\phi}\left(\frac{\cos\phi}{f}\frac{\partial}{\partial x}\right) + f^2\frac{\partial}{\partial p}\left(\frac{\partial}{\partial p}\right)\right]\Phi' \qquad , \qquad (7)$$

where q is the PV, ϕ is the geopotential, f is the Coriolis parameter, and a prime represents the deviation from the smoothed climatological annual cycle. We then inverted individual PV "pieces" at different
10   levels to evaluate near surface (850 hPa) horizontal wind anomalies related to these PV anomalies. The horizontal anomalous wind field that will be presented in Fig. 6 was derived from the geopotential height field based on geostrophic balance. We partitioned the 1000-100 hPa PV anomalies into the lower troposphere (1000-850 hPa) and the middle to upper troposphere (700-100 hPa) PV anomalies and compare their impacts on the near surface wind field in Sect. 3.

15   **3 Results**

3.1 Observation- and reanalysis-data based relationships among Arctic sea ice, atmospheric circulation, and boundary-layer ventilation

We first examined the long-term variations of Arctic sea ice in autumn and early winter (August to November, ASON) of the past four decades during the satellite era. Figure 1a shows the strong
20   decreasing trends in the Arctic sea ice extent, especially in the Eurasian and Pacific sectors such as the northern Barents Sea, Kara Sea, East Siberian Sea, and Chukchi Sea. The winter EU index shows positive correlations with the regional Arctic sea ice decline with the strongest correlation over the East Siberian Sea and Chukchi Sea (Fig. 1b). Positive correlations are also present when the long-term trend in regional sea ice changes is removed, suggesting a consistent relationship between EU variations and
25   sea ice changes in these Arctic regions on shorter (both interdecadal and interannual) time scales.

To evaluate the impact of EU phases on regional ventilation, we conducted composite analysis and compared wintertime boundary-layer PPI differences over the Northern Hemisphere corresponding to different EU phases. In general, PPI and EU show an in-phase relation with high (low) PPI anomalies corresponding to positive (negative) height anomalies in the EU pattern (Fig. 1c, d). Europe and East
30   Asia become two hot-spot regions in the negative EU phase (Fig. 1d), implying significant sensitivity (lower ventilation capability and higher air pollution potential) in these regions. Since the EU index shows a positive correlation with the declining sea ice in the Pacific sector of the Arctic, we would expect air stagnation to occur in the hot spot regions coinciding with the decrease of regional Arctic sea ice observed there.

3.2 WACCM sensitivity simulations

The statistical analysis suggests a potential linkage between the Arctic sea ice decline and the regional ventilation deterioration through a circulation change in the negative EU phase. We evaluated the teleconnection relationship using ensemble WACCM sensitivity experiments (Table 1). Figure 2 shows
5   the mean surface sensible plus latent heat flux changes between the SENSall and CTRL experiments during autumn and winter. Since we perturbed the Arctic SIC and SST in the model surface boundary conditions from August to November, most Arctic regions show significantly increased heat fluxes in autumn and early winter, especially over the Kara Sea, Laptev Sea, East Siberian Sea, and Beaufort Sea (Fig. 2a). The heat flux changes are much weaker in winter with some remnant influence over the Kara
10 Sea (Fig. 2b) due to the strong perturbation in this region. The comparison of monthly variations in regional averaged heat fluxes over the Arctic confirms the much stronger forcing in ASON (seasonal mean heat fluxes increased by 3.3 W/m^2 or +16% over the Arctic in SENSall) than in DJF (seasonal mean heat fluxes decreased by 0.17 W/m^2 or -1% over the Arctic in SENSall) (Fig. 2c). To examine the regional circulation and ventilation responses to these changes in the high latitudes, we fitted the CDF
15 and PDF curves of MCA_Z500 and ECP_PPI based on CTRL and SENS modeling results in winter. Figure 3 shows the CDF changes of simulated MCA_Z500 (Fig. 3a) and ECP_PPI indices (Fig. 3b) between sensitivity and CTRL experiments. It is clear that both indices show more significant changes in their extreme members than in medians or ensemble means, especially in SENSr2 driven by SIC and SST changes in the Pacific sector of the Arctic (R2 in Fig. 1b). In SENSr2, the occurrence probability of
20 MCA_Z500 positive extremes increases by 80% to 9% ± 3% (Fig. 3a; Table S3 in the Supplement), while the ECP_PPI positive extremes increases by 120% to 11% ± 3% (Fig. 3b; Table S3 in the Supplement). Meanwhile, the intensity of positive extreme values of both indices also increases by 26% and 32%, respectively (Table S4 in the Supplement). Such largely increased positive extremes in both indices of SENSr2 contribute to the positive responses in the ensemble means of two indices, making
25 SENSr2 the only sensitivity experiment with positive ensemble mean ECP_PPI. In comparison, other SENS experiments generally show negative ensemble mean ECP_PPI values due to negatively shifted CDF curves at most percentiles. For instance, both curves in SENSr1 driven by the regional SIC/SST perturbation in the Barents-Kara Seas (R1 in Fig. 1b) show complete shifts toward the left side with negative ensemble means and medians of MCA_Z500 and ECP_PPI indices as well as more negative
30 extremes at low quantiles and less positive extremes at high quantiles, suggesting an overall decrease of air stagnation and increase of regional ventilation driven by the SIC and SST changes in this region. The disparate results among the sensitivity experiments highlight distinct climate effects of regional SIC/SST changes as suggested by both statistical analysis in the last section and previous climate modeling studies. Screen (2017) and McKenna et al. (2018) investigated atmospheric responses to
35 regional sea ice loss by perturbing regional SIC and SST or surface temperature. McKenna et al. (2018) focused on the climate impacts of sea ice loss in the Atlantic (the Barents-Kara Seas) and the Pacific sectors (the Chukchi-Bering Seas) of the Arctic, while Screen (2017) conducted more comprehensive investigation by dividing the whole Arctic region into nine sub-regions. These region-specific modeling studies suggested quite different or even opposite effects of regional sea ice forcing on general
40 circulation in the stratosphere and troposphere. However, it is worth noting that they mainly focused on the responses in the stratospheric polar vortex and in the tropospheric Arctic Oscillation (AO) and North

Atlantic Oscillation (NAO), which are different from the EU and MCA_Z500 patterns of interest in this work.

The differences in the MCA_Z500 and ECP_PPI responses among the four sensitivity experiments in extreme members and ensemble means also suggest complex relationships between Arctic sea ice loss and mid-latitude weather changes. Two distinct patterns of Asian winter climate responses to Arctic sea ice loss were identified in a previous study (Wu et al., 2015), one (the "Siberian High" pattern) in positive phase associated with the strengthened Siberia High and EAWM systems while the other (the "Asia-Arctic" pattern) in negative phase associated with weakened EAWM and enhanced precipitation in East Asia. Such opposite responses in regional climate and weather systems partly explain the concurrent changes in the two tails of distribution curves in our sensitivity experiments. An IPCC report (IPCC, 2012) demonstrated three kinds of responses in variable probability distributions to climate change, and our ECP_PPI results in the four SENS experiments agree with the proposed "increased variability", "shifted mean", "changed symmetry", and "increased variability" responses, respectively (see section 2.3 and Table S2 and Fig. S3 in the Supplement for explanations). These distinct responses reflect complex interactions between atmospheric anomalies driven by climate forcing and atmospheric circulation associated with the natural variability. The coupling processes among different components of the climate system would compound such complexity by amplifying or dampening signal-to-noise ratios and expanding responsive regions (Deser et al., 2015; Deser et al., 2016). Smith et al. (2017) pointed out the importance of ocean-atmosphere coupling and the background state in modulating atmosphere responses to Arctic sea ice changes. They found that the background state plays a key role in determining the sign of the NAO responses to Arctic sea ice loss via the refraction of planetary waves by the climatological flow (Smith et al., 2017). These findings shed light on the diverse responses in our simulated distributions of MCA_Z500 and ECP_PPI because of the varying background flow in each modeling year. It is worth noting that we only changed the surface boundary conditions (SIC/SST) at these model grid cells with sea ice changes larger than 10% and kept other grid cells unperturbed. Because our study design used prescribed ocean data, the ice-ocean-atmosphere coupling is constrained and it might attenuate other atmospheric responses to sea ice changes as discussed in previous studies (Deser et al., 2015; Deser et al., 2016; Smith et al., 2017).

Considering air pollution responses, we found exacerbated haze pollution represented by positive anomalous $PM_{2.5}$ surface concentrations in eastern China regions concurrent with the ECP_PPI extreme values in all SENS experiments. The changes in surface $PM_{2.5}$ concentration fields correspond well with the PPI changes with the most significant increases in SENSr2 (Fig. S4 in the Supplement) due to the largest number of positive extreme members in this case (Fig. 3b). These positive PPI extremes in SENSr2 are attributed to both reduced surface wind speed and enhanced near surface temperature inversion (Fig. S5 in the Supplement). The agreement between PPI and surface $PM_{2.5}$ concentration changes demonstrates the promising capability of PPI for describing regional air stagnation and pollution potentials. Since the cause of increasing extreme events is the major concern of this work, we mainly focus on analyzing the dynamic processes contributing to the largest increase of ECP_PPI extremes in SENSr2 in the next section.

3.3 Diagnosis of dynamic processes

To elucidate the dynamic mechanisms of air stagnation extreme events driven by the Arctic sea ice forcing, we examined atmospheric responses induced by sea ice perturbations from the perspective of wave activity fluxes and transient eddy feedback forcing in winter over the Northern Hemisphere based on the SENSr2 extreme members. We also evaluated climate impacts of the anomalous circulations and teleconnection patterns in these extremes on regional ventilation using the piecewise PV inversion method. We first describe the anomalous geopotential height field in the upper troposphere (250 hPa, Fig. 4a) and sea level pressure anomalies (Fig. 4b), both of which share similar features with strong positive anomalies over the North Pacific and Northern Europe and negative ones over central Siberia. This quasi-barotropic structure over most regions of the Northern Hemisphere agrees with previous findings regarding Arctic sea ice induced atmospheric responses at interseasonal scales (Deser et al., 2010). The geopotential height anomalies in the upper troposphere manifest wave-train patterns with enhanced Rossby wave propagation from the North Pacific to North America and over the Eurasian continent (Fig. 4a). The sea level pressure anomalies exhibit eastward displacements with respect to the upper-troposphere anomalies over Eurasia (Fig. 4b). In particular, the negative sea level pressure anomaly over Siberia extends southeastward to southeastern China, suggesting a weakened Siberia High. In response, anomalous surface southerlies are seen along the coastal region of eastern China that offset the prevalent winter monsoon and thus increase the air stagnation in winter over eastern China.

We then compare the difference of EKE and **E** vectors (section 2.4) between SENSr2 extreme members and CTRL ensemble mean and calculated anomalous 250 hPa geopotential height tendencies driven by transient eddies using Eq. (5). The most prominent features in the anomalous zonal wind and transient eddy fields are zonal positive anomalies over the mid-latitudes from the northeastern Pacific to North Africa that are to the south of the upper-troposphere negative height anomalies (Fig. 4c). Meanwhile, both zonal wind and EKE fields feature a moderate dipole around the positive height anomaly. The divergence of **E** vectors is seen from the northeastern Pacific to the North Atlantic, which results in amplifications of zonal winds and a climatology-like pattern of transient eddy feedback forcing with zonally elongated positive height tendencies to the south of negative height tendencies (Fig. 4d). In contrast, the **E** vectors converge over the vicinity of the Scandinavian region (Fig. 4d), suggesting a weakened zonal wind and thereby depress transient eddy activity. Accordingly, significant geopotential height tendencies driven by transient eddy forcing emerge in the upper troposphere, showing pronounced positive anomalies near the Scandinavian region. These tendencies are dominated by transient eddy vorticity forcing rather than transient eddy heat forcing, the latter of which shows opposite but much weaker effects on the upper level geopotential height field (Fig. S6 in the Supplement). Both transient eddy vorticity and heat flux forcing contribute constructively in the lower troposphere (Fig. S6 in the Supplement).

We further compare the simulated atmosphere responses to the ensemble average of the 30 strongest negative EU years (10 minimums for each Dec/Jan/Feb month) in winter since 1950 in the reanalysis data. Figure 5 shows the horizontal (250 hPa) and vertical structures of wave propagation in reanalysis-based negative EU extremes and SENSr2 extreme members. They show similar features of wave train patterns with two anomalous troughs over the North Atlantic (region A in Fig. 5a, b) and the Siberian (region C in Fig. 5a, b) areas and two anomalous ridges over the Scandinavian Peninsula (region B in

Fig. 5a, b) and East Asia (region D in Fig. 5a, b) areas. These wave train patterns exhibit barotropic vertical structures in the troposphere in both cases (Fig. 5c, d). Unlike the reanalysis members, the wave train pattern of SENSr2 extreme members shows a westward tilt in the lower troposphere with evident downward energy propagation. To understand why more extreme members occurred in SENSr2 than
5 CTRL, we overlapped the vertical structure of the corresponding CTRL members (contours in Fig. 5d) to SENSr2 extreme members (shading in Fig. 5d) and compared their differences. Though these CTRL members share the same initial condition and similar vertical structures of wave train patterns with SENSr2 extreme members in upstream regions (e.g., the middle and upper troposphere over region B and C), a key difference emerges over the downstream region of East Asia (region D). Meanwhile, the
10 anomalous centers of CTRL members are higher than the SENSr2 extreme members and reanalysis counterparts, which is unfavorable for the lateral Rossby wave propagation to help the formation of the positive height anomalies over East Asia. In contrast to negative to neutral height anomalies in CTRL members, these SENSr2 extreme members manifest positive anomalies in the middle to upper troposphere over this region. This critical difference appears to be the key to more frequent ECP_PPI
15 extremes in the SENSr2 experiment.

To illustrate this point, we used the piecewise PV inversion method to examine the impact of the circulation anomalies in region D (the red box in Fig. 5a) on regional ventilation over eastern China in both the reanalysis and modeling data. We first partitioned tropospheric PV anomalies into two parts: the lower troposphere (1000-850 hPa) and the middle to upper troposphere (700-100 hPa) and then
20 inverted each PV piece at two levels to estimate the near-surface (850 hPa) horizontal anomalous winds associated with these PV anomalies. We find significantly weakened wind fields in eastern China in both data. In contrast to strong climatological northwesterly winds over northeastern Asia (Fig. 6a, b), PV anomalies in the middle to upper troposphere in both reanalysis-based negative EU and model-based SENSr2 extreme members induce anomalous southeasterly winds at the lower troposphere over
25 the East Asia coastal regions (Fig. 6c, d). These anomalous southeasterlies weaken the monsoon northwesterlies and strengthen air stagnation in this region. We also compare the contribution of PV anomalies at different levels and find that the ventilation suppression effect is dominated by anomalous PV in the middle to upper troposphere (700 hPa and above) rather than that in the lower troposphere (below 700 hPa) in both data. Comparing to anomalous southerly winds induced by PV anomalies in
30 middle to upper levels (Fig. 6c, d), those PV anomalies in the lower troposphere mainly tend to strengthen northerly climatological winds over the ECP region (Fig. 6e, f). In general, the ventilation suppression effect associated with middle and upper level circulation anomalies overwhelms the enhancement effect associated with lower level anomalies and suppresses monsoon winds as a net effect (Fig. 6g, h).

35 **3.4 Historical simulations and future projections in CMIP6**

Lastly, we examined the historical simulations and future projections of Arctic SIE and ECP_PPI under the SSP5-8.5 scenario based on 8 currently available CMIP6 climate models (Eying et al., 2016; see Table S1 in the Supplement for model details) to understand how this teleconnection relationship might change in the future. Figure 7 shows the time series of these two variables and the statistical distribution
40 changes of ECP_PPI among three time periods: P1 (1951-2000) as the reference period with slowly

declining Arctic SIE, P2 (2001-2050) as the near-term projection with rapidly decreasing Arctic SIE, and P3 (2051-2100) as the long-term projection with an almost ice-free Arctic in boreal Autumn. Although the CMIP6 model ensemble captures the observed decreasing trend in Arctic SIE, it generally shows less interannual and interdecadal variability of Arctic SIE and ECP_PPI than the reanalysis data.

5 Low decadal variations in the CMIP6 models are also evident in the CDF distributions of simulated ECP_PPI. For instance, the simulated ECP_PPI CDF curve in P1 is positively shifted over the whole distribution range in comparison with the reanalysis-based one (Fig. 7b), while the simulated CDF curve in P2 is negatively shifted relative to the reanalysis data (Fig. 7c) especially over the lower ends of the distribution. Therefore, the shift to positive PPI distributions from P1 to P2 in the NCEP

10 reanalysis data is much more significant than the CMIP6 ensemble. Consequently, the ensemble mean values and averaged probability of simulated ECP_PPI positive extremes increase from -0.05/5% in P1 to 0.07/7% in P2 (Fig. 7c), which is smaller than those presented in the reanalysis data (-0.38/5% in P1 to 0.30/19% in P2). With the greatest change of Arctic SIE in P3, the ensemble averaged probability of ECP_PPI positive extremes nearly doubles and increases to 9% with the ECP_PPI mean value of 0.09

15 (Fig. 7d), and the ensemble variance of ECP_PPI projections also increases substantially. The model-specific projections of positive extreme probabilities range between 2%-11% in P2, and between 2-13% in P3 (Table S5 and Fig. S7 in the Supplement).

For more direct comparison with the CESM-WACCM sensitivity results in previous sections, we specifically looked into the two newer versions of CESM (CESM2 and CESM2-WACCM; Table S1 in

20 the Supplement) that were developed in the same CESM project as the CESM-WACCM model used in this study. The ensemble mean and probability of positive extremes in the low-top CESM2 model increase from -0.07/5% in P1 to 0.20/11% in P2 and to 0.11/13% in P3, while these values in the high-top CESM2-WACCM model increase from 0.03/5% in P1 to 0.36/10% in P2 and to 0.27/6% in P3 (Table S5 and Fig. S7 in the Supplement). Both model results are much closer to the changes between

25 P1 and P2 shown in the reanalysis data than the other CMIP6 models. These increments are also more significant than the SENSall results of the sensitivity experiment in this study, which might be attributable to the much stronger climate forcing and fully coupled modeling settings in the CMIP6 simulations.

4 Discussion and conclusions

30 In this study, we revisited the connection between Arctic sea ice decline and winter air stagnation as a cause of pollution extremes in China. We identified a tropospheric pathway linking the remote sea ice changes in the Arctic to regional circulation and ventilation responses in eastern China based on statistical analysis and diagnosis of atmospheric dynamics using the NCEP reanalysis and climate model sensitivity simulation data. The teleconnection mechanism's evolution can be summarized as

35 follows: In autumn and early winter of recent years, sea ice declined greatly in most regions of the Arctic and significantly increased upward heat fluxes during the same period. These changes in surface boundary conditions, especially those that occurred in the Pacific sector of the Arctic (the East Siberian and Chukchi Seas), induced non-linear responses in the atmosphere during the following winter with strengthened eddy kinetic energy over the mid-latitudes from the northeastern Pacific to North Africa

and strong convergence of anomalous transient eddy vorticity fluxes over the vicinity of Scandinavia. This transient eddy forcing led to positive geopotential height tendencies as well as an anomalous ridge in this region throughout the troposphere. Constructive interference between eddy-induced wave packets and background flow enhanced wave train propagation across Eurasia, resembling the negative

5 phase of the EU pattern. The high-pressure anomalies over eastern Asia in the middle and upper troposphere of this teleconnection pattern finally weakened boundary-layer air ventilation and exacerbated air stagnation extremes in eastern China by suppressing monsoon northwesterlies and enhancing near surface temperature inversion in this region. Such meteorological conditions were favorable to air pollutant accumulation and secondary formation. The occurrence of these

10 teleconnection processes depends on complex interactions between climate disturbances and its internal variability, which are reflected by diverse climate sensitivity responses in the full statistical distributions of circulation and ventilation variables. The largest increase of both the probability (by 120%) and the intensity (by 32%) of air stagnation extreme events is found in the experiment driven by sea ice perturbations over the Pacific sector of the Arctic (the East Siberian and Chukchi Seas). We emphasize

15 the importance of a full-distribution evaluation, especially for extreme event assessment and attribution, considering vastly different responses between mean conditions and extremes and the tendency of underestimated impacts of climate extremes (Schewe et al., 2019). Next, we discuss some relevant aspects that deserve more attention and further investigations.

Firstly, Petoukhov et al. (2013) proposed a common physical mechanism for the generation of

20 regional summer weather extremes in the Northern Hemisphere through quasi-resonant amplification (QRA). They argued that these extreme-related persistent longitudinal planetary-scale high-amplitude circulation patterns with zonal wave numbers $m = 6$, 7, or 8 might result from the trapping of quasi-stationary free synoptic waves with zonal wave numbers $k \cong m$. These waveguides favor a subsequent strong QRA of the usually weak quasi-stationary response of wave numbers $m = 6\text{-}8$ to climatological

25 mean thermal and orographic forcing (Petoukhov et al., 2013). Several subsequent studies followed this analytical framework and demonstrated the critical role of QRA in recent warm-season extreme weather events (Coumou et al., 2014; Kornhuber et al., 2017; Petoukhov et al., 2016). Though the EU teleconnection pattern with zonal wave number $m = 3$ in this work does not support their hypothesis, the working mechanism through wave interference could be similar as shown in Fig. 5d. It is noted that

30 atmospheric circulation patterns like EU with smaller wave numbers might be excited by quasi-stationary spatially inhomogeneous diabatic sources/sinks and orography other than the thermal forcing associated with the SIC/SST perturbation used in this study. Therefore, we mainly focus on the relative changes of teleconnection occurrence probability between the CTRL and sensitivity experiments to isolate the contributions from this single forcing in the simulated atmospheric system. Multiple

35 atmospheric processes and various forcing source regions associated with different teleconnection pathways might increase the detection difficulty in the whole Arctic perturbation experiment.

Secondly, the climate impacts may vary in response to differing location and magnitude of climate forcing as we found in our regional sensitivity experiments and as often discussed in other modeling studies (Screen, 2017; Sun et al., 2015; McKenna et al., 2018). The different responses might be

40 attributable to different mechanisms and atmospheric processes associated with specific forcing-response relationships. Previous studies proposed multiple pathways of Arctic sea ice impacts on middle-latitude atmospheric circulation through troposphere-stratosphere coupling and/or tropospheric

processes only. It is an intriguing question to quantify the relative importance of different pathways in different case studies. Screen (2017) proposed that a stratosphere pathway dominated the atmosphere responses to sea ice loss in the Barents-Kara Seas whereas tropospheric processes governed wave train responses to sea ice loss in other regions, which is partly consistent with what we found in this study.

5 Similarly, McKenna et al. (2018) also found opposite effects of the regional sea ice forcing on the stratospheric polar vortex in their full-magnitude and half-magnitude forcing experiments, but the tropospheric responses were different between the two experiments with different forcing magnitudes. They suggested that tropospheric processes become more important than stratospheric pathways as the sea ice loss magnitude increases (McKenna et al., 2018). Our modeling results indicate that the

10 tropospheric processes are the key to understand the force-response relationship of interest. However, we can not rule out the possible role of stratospheric changes in midlatitude weather extreme events through stratosphere-troposphere coupling processes (Zhang et al., 2018), and the CESM2 model's sensitivity appears to be stronger when the stratosphere is reasonably resolved in its high-top WACCM version. More detailed sensitivity experiments need to be designed and conducted to evaluate such

15 pathway-dependent effects of Arctic sea ice loss on regional circulation and pollution conditions.

Thirdly, climate responses to Arctic sea ice forcing may also vary on intra-seasonal scales. In a recent study, Lu et al. (2019) revealed an important role of the autumn Arctic sea ice in the phase reversal of the Siberian high in November and December-January. They suggested that the autumn Arctic sea ice loss, especially in the Barents Sea, could induce anomalous upward (downward) surface

20 turbulent heat fluxes in November (December-January). This would strengthen (weaken) the development of the storm track in northeastern Europe and decrease (increase) Ural blockings with accelerated (decelerated) westerlies. With inhibited (enhanced) cold air transport from the Arctic to the Siberian area, a weaker (stronger) Siberian high in November (December-January) would occur thereafter. In our modeling results, we also found significant intra-seasonal variations in simulated

25 atmosphere responses. Figure S8 in the Supplement shows weekly evolution of geopotential height tendencies and anomalies in SENSr2 from late November to February. The negative phases of the EU pattern are more prominent in early winter than in late winter. Better understanding of such intra-seasonal variations could benefit seasonal and sub-seasonal forecasts of regional ventilation and pollution potentials.

30 Last but not the least, concurrence of multiple climate drivers and their synergistic climate impacts should be considered. Since many other climate factors such as Eurasian snow cover, ENSO, and PDO also show considerable influence on regional circulation and air pollution in China (Chang et al., 2016; Sun et al., 2018; Zhao et al., 2016; Zhao et al., 2018; Zhang et al., 2019; Zou et al., 2017), more studies with concurrent climate drivers could be conducted for comprehensive understanding of climate change

35 impacts. However, these climate drivers may interact with each other with both synergistic or antagonistic effects (Li et al., 2019). Active sea ice-ocean-atmosphere coupling also allows more sophisticated dynamic and thermodynamic feedbacks with expanded and enhanced climate responses as suggested by previous studies (Deser et al., 2015; Smith et al., 2017) and by the CMIP6 fully coupled projections in this study. Furthermore, the Arctic sea ice cover reached its historical minimum in the fall

40 of 2012 (Fig. 7a; NSIDC/NASA, 2019). The slowdown of Arctic sea ice loss since then may reflect regional climate internal variability and may have weakened the effect of the Arctic sea ice loss on winter extreme haze occurrence in China in recent years.

Data availability

The NCEP Reanalysis data is provided by the NOAA/OAR/ESRL PSD, Boulder, Colorado, USA, from their web site at https://www.esrl.noaa.gov/psd/data/gridded/data.ncep.reanalysis.html. The MEIC-MIX emission inventory data is available at http://www.meicmodel.org/dataset-mix. The CMIP6 model outputs are distributed by the Earth System Grid Federation (ESGF) at https://esgf-node.llnl.gov/search/cmip6/. All the modeling output data reported in the paper are tabulated in the main text and archived on the GLADE and HPSS file systems managed by the Computational & Information Systems Lab (CISL) of NCAR. The modeling source code and data materials are available upon request, which should be addressed to YZ (yufei.zou@pnnl.gov).

Author contributions

YZ and YW conceived the research idea and designed the climate sensitivity experiments. YZ conducted the modeling experiments and analyzed modeling results with ZX. YZ prepared all the figures and wrote the draft manuscript. All authors discussed the results and revised the manuscript.

Competing interests.

The authors declare no conflict of interest.

Acknowledgements

We acknowledge high-performance computing support from Yellowstone (ark:/85065/d7wd3xhc) and Cheyenne (doi:10.5065/D6RX99HX) provided by NCAR's CISL, sponsored by the National Science Foundation. We thank the Physical Sciences Division (PSD) at the NOAA Earth System Research Laboratory (ESRL) for providing the NCEP/NCAR Reanalysis data. We thank the MEIC team for providing the MEIC-MIX emission inventory data. We acknowledge the World Climate Research Programme, which, through its Working Group on Coupled Modelling, coordinated and promoted CMIP6. We thank the climate modeling groups for producing and making available their model output, the Earth System Grid Federation (ESGF) for archiving the data and providing access, and the multiple funding agencies who support CMIP6 and ESGF. We thank DOE's RGMA program area, the Data Management program, and NERSC for making this coordinated CMIP6 analysis activity possible. We are also thankful to Robert Black, Yi Deng, and Jian Lu for their helpful discussion to improve the data analysis in this paper.

Financial support

This work is supported by the National Science Foundation Atmospheric Chemistry Program. ZX is supported by the National Natural Science Foundation of China (project number: 41861144014). YZ,

HW, and PR are supported by the U.S. Department of Energy (DOE) Office of Science Regional and Global Model Analysis (RGMA) Program. The Pacific Northwest National Laboratory (PNNL) is operated for DOE by Battelle Memorial Institute under contract DE-AC05-76RL01830. It has not been subjected to any agency review and therefore does not necessarily reflect the views of the Foundation,
5   and no official endorsement should be inferred.

References

An, Z., Huang, R.J., Zhang, R., Tie, X., Li, G., Cao, J., Zhou, W., Shi, Z., Han, Y., Gu, Z. and Ji, Y.: Severe haze in Northern China: A synergy of anthropogenic emissions and atmospheric
10   processes, P. Natl. Acad. Sci. USA, 116, 8657-8666, https://doi.org/10.1073/pnas.190012511, 2019.

Black, R. X., and McDaniel, B. A.: Diagnostic case studies of the northern annular mode, J. Climate, 17, 3990–4004, 2004.

Cai, W. J., Li, K., Liao, H., Wang, H. J., and Wu, L. X.: Weather conditions conducive to Beijing
15   severe haze more frequent under climate change, Nat. Clim. Change, 7, 257-+, 2017.

Chang, L., Xu, J., Tie, X., and Wu, J.: Impact of the 2015 El Nino event on winter air quality in China, Scientific Reports, 6(1), 34275, https://doi.org/10.1038/srep34275, 2016.

Cheng, Y., Zheng, G., Wei, C., Mu, Q., Zheng, B., Wang, Z., Gao, M., Zhang, Q., He, K., Carmichael, G. and Pöschl, U.: Reactive nitrogen chemistry in aerosol water as a source of sulfate during
20   haze events in China. Science Advances, 2, e1601530, 2016.

Cohen, J., Screen, J. A., Furtado, J. C., Barlow, M., Whittleston, D., Coumou, D., Francis, J., Dethloff, K., Entekhabi, D., Overland, J., and Jones, J.: Recent Arctic amplification and extreme mid-latitude weather, Nat. Geosci. 7, 627-637, 2014.

Coumou, D., Petoukhov, V., Rahmstorf, S., Petri, S. and Schellnhuber, H.J.: Quasi-resonant circulation
25   regimes and hemispheric synchronization of extreme weather in boreal summer. P. Natl. Acad. Sci. USA, 111(34), 12331-12336, https://doi.org/10.1073/pnas.1412797111, 2014

Dawson, J. P., Bloomer, B. J., Winner, D. A., and Weaver, C. P.: Understanding the meteorological drivers of U.S. particulate matter concentrations in a changing climate, B. Am. Meteorol. Soc., 521-532, https://doi.org/10.1175/BAMS-D-12-00181.1, 2014.

30   Deser, C., Sun, L. T., Tomas, R. A., and Screen, J.: Does ocean coupling matter for the northern extratropical response to projected Arctic sea ice loss? Geophys. Res. Lett., 43, 2149-2157, 2016.

Deser, C., Tomas, R., Alexander, M., and Lawrence, D.: The seasonal atmospheric response to projected Arctic sea ice loss in the late twenty-first century. J. Climate, 23, 333–351,
35   doi:10.1175/2009JCLI3053.1, 2010.

Deser, C., Tomas, R. A., and Sun, L. T.: The role of ocean–atmosphere coupling in the zonal-mean atmospheric response to Arctic sea ice loss, J. Climate, 28, 2168-2186, doi:10.1175/JCLI-D-14-00325.1, 2015.

Eyring, V., Bony, S., Meehl, G. A., Senior, C. A., Stevens, B., Stouffer, R. J., and Taylor, K. E.:
Overview of the Coupled Model Intercomparison Project Phase 6 (CMIP6) experimental design
and organization, Geosci. Model Dev., 9, 1937-1958, doi:10.5194/gmd-9-1937-2016, 2016

Geng, G., Zhang, Q., Tong, D., Li, M., Zheng, Y., Wang, S., and He, K.: Chemical composition of
ambient PM2:5 over China and relationship to precursor emissions during 2005–2012, Atmos.
Chem. Phys., 17, 9187-9203, https://doi.org/10.5194/acp-17-9187-2017, 2017.

Guo, S., Hu, M., Zamora, M.L., Peng, J., Shang, D., Zheng, J., Du, Z., Wu, Z., Shao, M., Zeng, L. and
Molina, M.J.: Elucidating severe urban haze formation in China. P. Natl. Acad. Sci. USA, 111,
17373-17378, 2014.

Horton, D. E., Skinner, C. B., Singh, D., and Diffenbaugh, N. S.: Occurrence and persistence of future
atmospheric stagnation events, Nat. Clim. Change, 4, 698-703, 2014.

Hoskins, B. J., James, I. N., and White, G. H.: The shape, propagation and mean-flow interaction of
large-scale weather systems, J. Atmos. Sci., 40, 1595-1612, 1983.

Huang, R. J., Zhang, Y., Bozzetti, C., Ho, K. F., Cao, J. J., Han, Y., Daellenbach, K. R., Slowik, J. G.,
Platt, S. M., Canonaco, F., Zotter, P., Wolf, R., Pieber, S. M., Bruns, E. A., Crippa, M., Ciarelli,
G., Piazzalunga, A., Schwikowski, M., Abbaszade, G., Schnelle-Kreis, J., Zimmermann, R., An,
Z., Szidat, S., Baltensperger, U., El Haddad, I., Prévôt, A. S.: High secondary aerosol
contribution to particulate pollution during haze events in China, Nature, 514, 218-222, 2014.

IPCC, Field, C.B., Barros, V., Stocker, T.F., Qin, D., Dokken, D.J., Ebi, K.L., Mastrandrea, M.D.,
Mach, K.J., Plattner, G.-K., Allen, S.K., Tignor, M., and Midgley, P.M. (eds.): Managing the
risks of extreme events and disasters to advance climate change adaptation. A special report of
working groups I and II of the Intergovernmental Panel on Climate Change. Cambridge
University Press, Cambridge, UK, and New York, NY, USA, 582 pp, 2012.

IPCC, Pörtner, H.-O., Roberts, D.C., Masson-Delmotte, V., Zhai, P., Tignor, M., Poloczanska, E.,
Mintenbeck, K., Nicolai, M., Okem, A., Petzold, J., Rama, B., and Weyer, N. (eds.): Summary
for Policymakers. In: IPCC Special Report on the Ocean and Cryosphere in a Changing Climate.
In press, 2019.

Jia, B., Wang, Y., Yao, Y., and Xie, Y.: A new indicator on the impact of large-scale circulation on
wintertime particulate matter pollution over China, Atmos. Chem. Phys., 15, 11919-11929,
2015.

Kalnay, E., Kanamitsu, M., Kistler, R., Collins, W., Deaven, D., Gandin, L., Iredell, M., Saha, S.,
White, G., Woollen, J., Zhu, Y., Chelliah, M., Ebisuzaki, W., Higgins, W., Janowiak, J., Mo, K.
C., Ropelewski, C., Wang, J., Leetmaa, A., Reynolds, R., Jenne, R., and Joseph, D.: The
NCEP/NCAR 40-year reanalysis project, B. Am. Meteorol. Soc., 77, 437-471,
doi:10.1175/1520-0477(1996)077<0437:Tnyrp>2.0.Co;2, 1996.

Kan, H. D., Chen, R. J., and Tong, S. L.: Ambient air pollution, climate change, and population health
in China, Environ. Int., 42, 10-19, 2012.

Kornhuber, K., Petoukhov, V., Petri, S., Rahmstorf, S. and Coumou, D.: Evidence for wave resonance
as a key mechanism for generating high-amplitude quasi-stationary waves in boreal summer.
Clim. Dyn., 49, 1961-1979, https://doi.org/10.1007/s00382-016-3399-6, 2017.

Lamarque, J. F., Bond, T. C., Eyring, V., Granier, C., Heil, A., Klimont, Z., Lee, D., Liousse, C.,
Mieville, A., Owen, B., Schultz, M. G., Shindell, D., Smith, S. J., Stehfest, E., Van Aardenne, J.,

Cooper, O. R., Kainuma, M., Mahowald, N., McConnell, J. R., Naik, V., Riahi, K., and van Vuuren, D. P.: Historical (1850-2000) gridded anthropogenic and biomass burning emissions of reactive gases and aerosols: methodology and application, Atmos. Chem. Phys., 10, 7017-7039, 10.5194/acp-10-7017-2010, 2010.

5   Lau, N.-C. and Holopainen, E. O.: Transient eddy forcing of the time-mean flow as identified by geopotential tendencies, J. Atmospheric Sci., 41, 313-328, https://doi.org/10.1175/1520-0469, 1984.

Lau, N.-C. and Nath, M. J.: Variability of the baroclinic and barotropic transient eddy forcing associated with monthly changes in the midlatitude storm tracks, J. Atmospheric Sci., 48, 2589-2613, 1991.

10 Li, B. G., Gasser, T., Ciais, P., Piao, S., Tao, S., Balkanski, Y., Hauglustaine, D., Boisier, J.-P., Chen, Z., Huang, M., Li, L. Z., Li, Y., Liu, H., Liu, J., Peng, S., Shen, Z., Sun, Z., Wang, R., Wang, T., Yin, G., Yin, Y., Zeng, H., Zeng, Z., and Zhou, F.,: The contribution of China's emissions to global climate forcing, Nature, 531, 357-+, 2016.

Li, J., Zheng, F., Sun, C., Feng, J. and Wang, J.: Pathways of influence of the Northern Hemisphere
15   mid-high latitudes on East Asian climate: A review. Adv. Atmos. Sci., 36, 902-921, https://doi.org/10.1007/s00376-019-8236-5, 2019.

Li, M., Zhang, Q., Kurokawa, J.-i., Woo, J.-H., He, K., Lu, Z., Ohara, T., Song, Y., Streets, D. G., Carmichael, G. R., Cheng, Y., Hong, C., Huo, H., Jiang, X., Kang, S., Liu, F., Su, H., and Zheng, B.: MIX: a mosaic Asian anthropogenic emission inventory under the international
20   collaboration framework of the MICS-Asia and HTAP, Atmos. Chem. Phys., 17, 935-963, https://doi.org/10.5194/acp-17-935-2017, 2017.

Li, Y., Sheng, L., Li, C. and Wang, Y.: Impact of the Eurasian teleconnection on the interannual variability of haze-fog in northern China in January, Atmosphere, 10, 113, 2019.

Liu, J., Mauzerall, D. L., Chen, Q., Zhang, Q., Song, Y., Peng, W., Klimont, Z., Qiu, X., Zhang, S., Hu,
25   M., Lin, W., Smith, K. R., and Zhu, T.: Air pollutant emissions from Chinese households: A major and underappreciated ambient pollution source, P. Natl. Acad. Sci. USA, 113, 7756-7761, 2016.

Liu, Y., Wang, L., Zhou, W., and Chen, W.: Three Eurasian teleconnection patterns: spatial structures, temporal variability, and associated winter climate anomalies, Clim. Dyn., 42, 2817-2839,
30   DOI:10.1007/s00382-014-2163-z, 2014.

Lou, S., Yang, Y., Wang, H., Smith, S. J., Qian, Y., and Rasch, P. J.: Black carbon amplifies haze over the North China Plain by weakening the East Asian winter monsoon. Geophysical Research Letters, 46(1), 452-460, DOI: 10.1029/2018GL080941, 2019.

Lu, Z., He, S., Li, F., and Wang, H.: Impacts of the autumn Arctic sea ice on the intraseasonal reversal
35   of the winter Siberian High, Adv. Atmos. Sci., DOI: 10.1007/s00376-017-8089-8, 2019.

Mann, M.E., Rahmstorf, S., Kornhuber, K., Steinman, B.A., Miller, S.K., Petri, S. and Coumou, D.. Projected changes in persistent extreme summer weather events: The role of quasi-resonant amplification. Science advances, 4(10), p.eaat3272, 2018.

Marsh, D. R., Mills, M. J., Kinnison, D. E., and Lamarque, J.-F.: Climate Change from 1850 to 2005
40   Simulated in CESM1(WACCM), J. Climate, 26, 7372-7391, 2013.

McKenna, C. M., Bracegirdle, T. J., Shuckburgh, E. F., Haynes, P. H., Joshi, M. M.: Arctic sea-ice loss in different regions leads to contrasting Northern Hemisphere impacts, Geophys. Res. Lett., https://doi.org/10.1002/2017GL076433, 2018.

Niu, F., Li, Z. Q., Li, C., Lee, K. H., and Wang, M. Y.: Increase of wintertime fog in China: Potential impacts of weakening of the Eastern Asian monsoon circulation and increasing aerosol loading, J Geophys Res-Atmos., 115, 2010.

National Snow and Ice Data Center (NSIDC): Quick facts on Arctic sea ice, https://nsidc.org/cryosphere/quickfacts/seaice.html, last access: 15 October, 2019

NSIDC/NASA: Arctic sea ice minimum, https://climate.nasa.gov/vital-signs/arctic-sea-ice/, last access: 18 July, 2019

Pei, L., Yan, Z., Sun, Z., Miao, S., and Yao, Y.: Increasing persistent haze in Beijing: potential impacts of weakening East Asian winter monsoons associated with northwestern Pacific sea surface temperature trends, Atmos. Chem. Phys., 18, 3713-3183, https://doi.org/10.5194/acp-18-3173-2018, 2018.

Petoukhov, V., Rahmstorf, S., Petri, S. and Schellnhuber, H.J.: Quasiresonant amplification of planetary waves and recent Northern Hemisphere weather extremes, P. Natl. Acad. Sci. USA, 110, 5336-5341, https://doi.org/10.1073/pnas.1222000110, 2013.

Petoukhov, V., Petri, S., Rahmstorf, S., Coumou, D., Kornhuber, K. and Schellnhuber, H.J.: Role of quasiresonant planetary wave dynamics in recent boreal spring-to-autumn extreme events. P. Natl. Acad. Sci. USA, 113, 6862-6867, https://doi.org/10.1073/pnas.1606300113, 2016.

Rayner, N. A., Parker, D. E., Horton, E. B., Folland, C. K., Alexander, L. V., Rowell, D. P., Kent, E. C., and Kaplan, A.: Global analyses of sea surface temperature, sea ice, and night marine air temperature since the late nineteenth century, J. Geophys. Res-Atmos., 108, 2003.

Schewe, J., Gosling, S.N., Reyer, C., Zhao, F., Ciais, P., Elliott, J., Francois, L., Huber, V., Lotze, H.K., Seneviratne, S.I. and Van Vliet, M.T.: State-of-the-art global models underestimate impacts from climate extremes. Nature communications, 10, 1005, https://doi.org/10.1038/s41467-019-08745-6, 2019.

Screen, J. A.: Simulated atmospheric response to regional and pan-Arctic sea ice loss, J. Climate, 30, 3945-3962, 2017.

Screen, J. A., Simmonds, I., Deser, C., and Tomas, R.: The atmospheric response to three decades of observed arctic sea ice loss, J. Climate, 26, 1230-1248, DOI: 10.1175/JCLI-D-12-00063.1, 2013.

Sun, J., Li, H., Zhang, W., Li, T., Zhao, W., Zuo, Z., Guo, S., Wu, D., Fan, S.: Modulation of the ENSO on winter aerosol pollution in the eastern region of China, J. Geophys. Res-Atmos., 123, https://doi.org/10.1029/2018JD028534, 2018.

Sun, L., Deser, C., and Tomas, R.A.: Mechanisms of stratospheric and tropospheric circulation response to projected Arctic sea ice loss, J. Climate, 28, 7824-7845, DOI: 10.1175/JCLI-D-15-0169.1, 2015.

Sun, Y. L., Du,W., Fu, P., Wang, Q., Li, J., Ge, X., Zhang, Q., Zhu, C., Ren, L., Xu, W., Zhao, J., Han, T., Worsnop, D. R., and Wang, Z.: Primary and secondary aerosols in Beijing in winter: sources, variations and processes, Atmos. Chem. Phys., 16, 8309-8329, 2016.

Takaya, K., and Nakamura, H.: A formulation of a phase-independent wave-activity flux for stationary and migratory quasigeostrophic eddies on a zonally varying basic flow, J. Atmos. Sci., 58, 608-627, 2001.

Taylor, K. E., Stouffer, R. J., and Meehl, G. A.: An Overview of Cmip5 and the Experiment Design, B. Am. Meteorol. Soc., 93, 485-498, 2012.

The State Council of the People's Republic of China: Notice on the air pollution prevention and control action plan, <http://www.gov.cn/zwgk/2013-09/12/content_2486773.htm> (2013).

Trenberth, K. E.: An assessment of the impact of transient eddies on the zonal flow during a blocking episode using localized Eliassen-Palm flux diagnostics, J. Atmos. Sci., 43, 2070-2087, 1986.

Wallace, J. M. and Gutzler, D. S.: Teleconnections in the geopotential height field during the Northern Hemisphere winter, Mon. Weaterh Rev., 109, 784-812, 1981.

Wang, G. H., Zhang, R., Gomez, M. E., Yang, L., Zamora, M. L., Hu, M., Lin, Y., Peng, J., Guo, S., Meng, J., Li, J., Cheng, C., Hu, T., Yanqin Ren, Y., Wang, Y., Gao, J., Cao, J., An, Z., Zhou, W., Li, G., Wang, J., Tian, P., Marrero-Ortiz, W., Secrest, J., Du, Z., Zheng, J., Shang, D., Zeng, L., Shao, M., Wang, W., Huang, Y., Wang, Y., Zhu, Y., Li, Y., Hu, J., Pan, B., Cai, L., Cheng, Y., Ji, Y., Zhang, F., Rosenfeld, D., Liss, P. S., Duce, R. A., Kolb, C. E., and Molina, M. J.: Persistent sulfate formation from London fog to Chinese haze, P. Natl. Acad. Sci. USA, 113, 13630-13635, 2016.

Wang, H. J., and Chen, H.-P.: Understanding the recent trend of haze pollution in eastern China: roles of climate change, Atmos. Chem. Phys., 16, 4205-421, 2016.

Wang, H. J., Chen, H. P., and Liu, J. P.: Arctic sea ice decline intensified haze pollution in eastern China, Atmos. Ocean. Sci. Lett., 8, 1–9, 2015.

Wang, N. and Zhang, Y.: Evolution of Eurasian teleconnection pattern and its relationship to climate anomalies in China, Clim. Dyn., 45, 1017-1028, DOI:10.1007/ s00382-014-2171-z, 2015.

Wilks, D. S.: Statistical methods in the atmospheric sciences. International geophysics series, ed. 3rd, Academic Press, Oxford Waltham, MA, pp. xix, 676 p, 2011.

Wu, B., Su, J., and D'Arrigo, R.: Patterns of Asian winter climate variability and links to Arctic sea ice, J. Climate, 28, 6841-6858, 2015.

Xie, Y., Dai, H. C., Dong, H. J., Hanaoka, T., and Masui, T.: Economic impacts from PM2.5 pollution-related health effects in China: A provincial-level analysis, Environ. Sci. Technol., 50, 4836-4843, 2016.

Yin, Z. and Wang, H.: Role of atmospheric circulations in haze pollution in December 2016, Atmos. Chem. Phys., 17, 11673-11681, 2017.

Yin, Z. and Wang, H. J.: The strengthening relationship between Eurasian snow cover and December haze days in central North China after the mid-1990s, Atmos. Chem. Phys., 18, 4753-4763, https://doi.org/10.5194/acp-18-4753-2018, 2018.

Zhao, S., Zhang, H., and Xie, B.: The effects of El Niño–Southern Oscillation on the winter haze pollution of China. Atmos. Chem. Phys., 18, 1863–1877. https://doi.org/10.5194/acp-18-1863-2018, 2018.

Zhao, S., Li, J., and Sun, C.: Decadal variability in the occurrence of wintertime haze in central eastern China tied to the Pacific Decadal Oscillation, Scientific Reports, 6(1), 27424, https://doi.org/10.1038/srep27424, 2016.

Zhang, P., Wu, Y., Simpson, I.R., Smith, K.L., Zhang, X., De, B. and Callaghan, P.: A stratospheric pathway linking a colder Siberia to Barents-Kara Sea sea ice loss. Science advances, 4, eaat6025, https://doi.org/10.1126/sciadv.aat6025, 2018.

Zhang, G., Gao, Y., Cai, W., Leung, L. R., Wang, S., Zhao, B., Wang, M., Shan, H., Yao, X., and Gao, H.: Seesaw haze pollution in North China modulated by the sub-seasonal variability of atmospheric circulation, Atmos. Chem. Phys., 19, 565-576, https://doi.org/10.5194/acp-19-565-2019, 2019.

Zhang, X., Zhong, J., Wang, J., Wang, Y., and Liu, Y.: The interdecadal worsening of weather conditions affecting aerosol pollution in the Beijing area in relation to climate warming, Atmos. Chem. Phys., 18, 5991-5999, https://doi.org/10.5194/acp-18-5991-2018, 2018.

Zhong, J., Zhang, X., Dong, Y., Wang, Y., Liu, C., Wang, J., Zhang, Y., and Che, H.: Feedback effects of boundary-layer meteorological factors on cumulative explosive growth of PM2.5 during winter heavy pollution episodes in Beijing from 2013 to 2016, Atmos. Chem. Phys., 18, 247-258, https://doi.org/10.5194/acp-18-247-2018, 2018.

Zou, Y., Wang, Y., Zhang, Y., and Koo, J.-H.: Arctic sea ice, Eurasia snow, and extreme winter haze in China, Science Advances, 3, e1602751, https://doi.org/10.1126/sciadv.1602751, 2017.

Table 1. The modeling settings of the climate sensitivity experiments using CESM-WACCM

Experiment	CTRL	SENSall	SENSr1	SENSr2	SENSr3
Time period	30 years	30 years	30 years	30 years	30 years
Horizontal resolution	1.9°×2.5°	1.9°×2.5°	1.9°×2.5°	1.9°×2.5°	1.9°×2.5°
Vertical level	70	70	70	70	70
Atmosphere	WACCM[a]	WACCM	WACCM	WACCM	WACCM
Land	CLM4.0	CLM4.0	CLM4.0	CLM4.0	CLM4.0
Ocean	Climatology[b]	2012 Arctic SST	2012 R1 SST[c]	2012 R2 SST	2012 R3 SST
Sea ice	Climatology[b]	2012 Arctic SIC	2012 R1 SIC	2012 R2 SIC	2012 R3 SIC
China emissions	MEIC-MIX	MEIC-MIX	MEIC-MIX	MEIC-MIX	MEIC-MIX
Other emissions	IPCC AR5	IPCC AR5	IPCC AR5	IPCC AR5	IPCC AR5

[a]: using CAM5 physics package and WACCM_MOZART_MAM3 chemistry package;

[b]: 1981-2010 average based on the HadISST SST and SIC data (Rayner et al., 2003);

5   [c]: see the main text and Fig. 1b for the R1-R3 region definition;
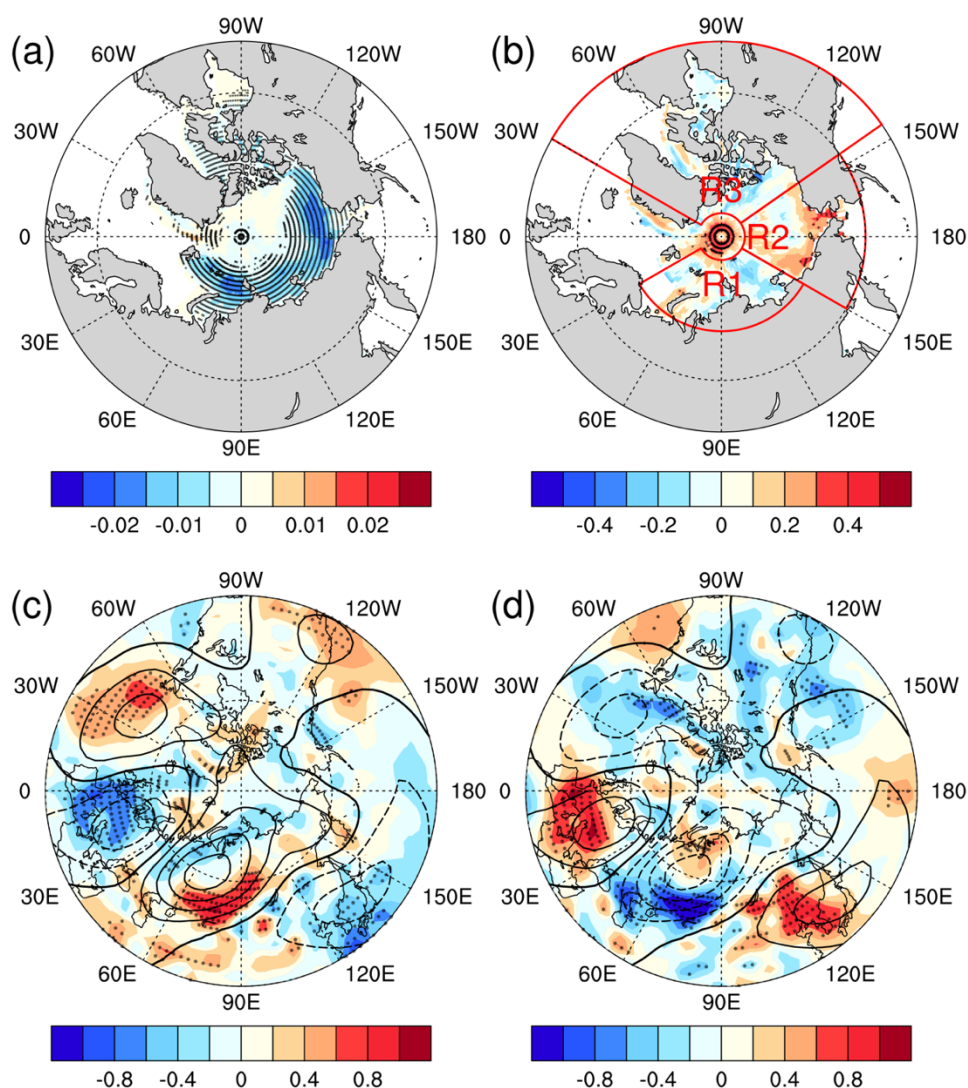
Figure 1. Relationship between Arctic sea ice changes, EU teleconnection, and pollution ventilation conditions in the Northern Hemisphere. (a) trends of Arctic sea ice changes in autumn and early winter (ASON) of 1980-2017 (color shading in the Arctic region, year^{-1}); (b) correlation between the EU index and Arctic sea ice concentrations (color shading in the Arctic region, unitless); R1-3 denote the perturbation regions in the three region-specific sensitivity experiments; (c) PPI spatial distributions (color shading, unitless) during the positive phase of EU (contours with interval of 20 m; dashed/solid lines indicate negative/positive geopotential heights at 500 hPa); (d) PPI spatial distributions (color shading, unitless) during the negative phase of EU (contours with interval of 20 m; dashed/solid lines indicate negative/positive geopotential heights at 500 hPa). The black dots over color shading denote the 0.05 significance level based on the two-tailed Student's t-test.
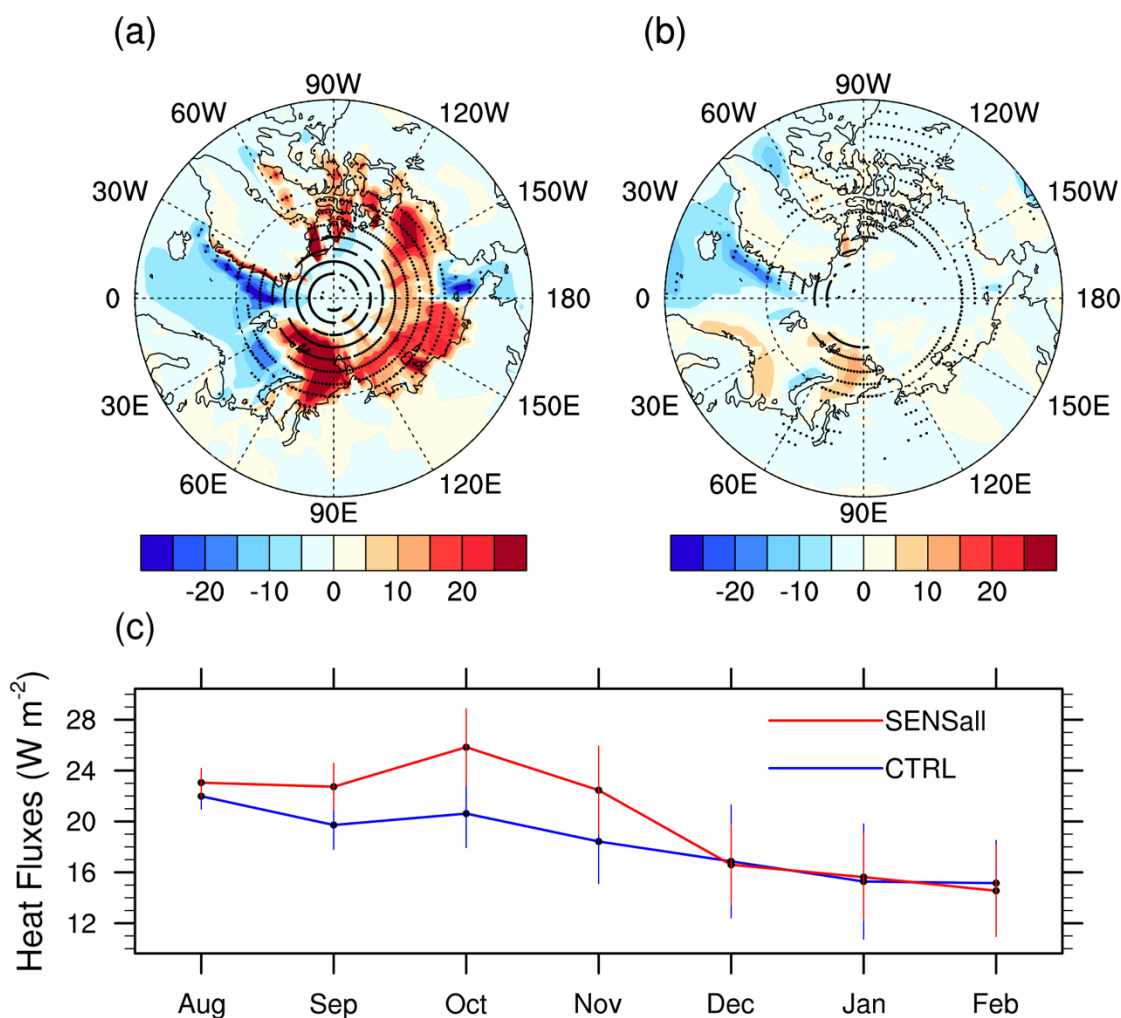
Figure 2. Surface heat flux changes over the Arctic in the WACCM SENSall simulation. (a) differences of surface sensible plus latent heat fluxes (positive upward) between SENSall and CTRL during Aug-Nov; (b) differences of surface sensible plus latent heat fluxes between SENSall and CTRL during Dec-Feb; (c) comparison of regional averaged surface heat fluxes over the Arctic (north of 66.6° N) from August to February. The black dots in (a)/(b) denote the 0.05 significance level. The error bars in (c) denote one standard deviation of the 30-member ensembles in CTRL and SENSall, respectively.
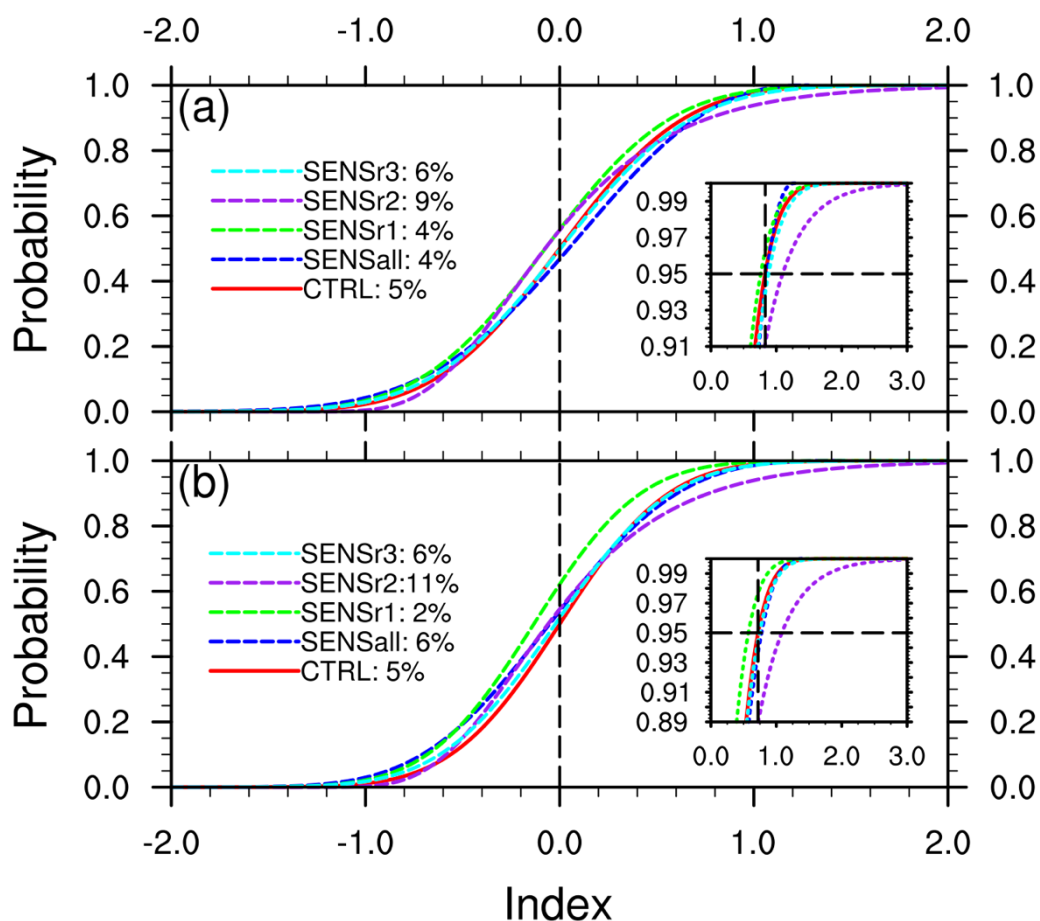
Figure 3. Atmospheric circulation and regional air stagnation responses to the Arctic sea ice forcing in the WACCM experiments. (a) comparison of cumulative distribution functions (CDFs) of the MCA_Z500 index in winter months (Dec, Jan, and Feb). The percentages in the legend are the occurrence probabilities of positive extreme members; the inset shows the zoomed-in distributions of positive MCA_Z500 extremes ($\geq MCA\_Z500_{CTRL}^{95^{th}}$) and the black dashed lines in the inlet denote the positive extreme threshold ($MCA\_Z500_{CTRL}^{95^{th}} = 0.83$); (b) same as (a) but for the regional averaged ECP_PPI index; the inset shows the zoomed-in distributions of positive PPI extremes ($\geq ECP\_PPI_{CTRL}^{95^{th}}$) and the black dashed lines in the inlet denote the positive extreme threshold ($ECP\_PPI_{CTRL}^{95^{th}} = 0.72$).
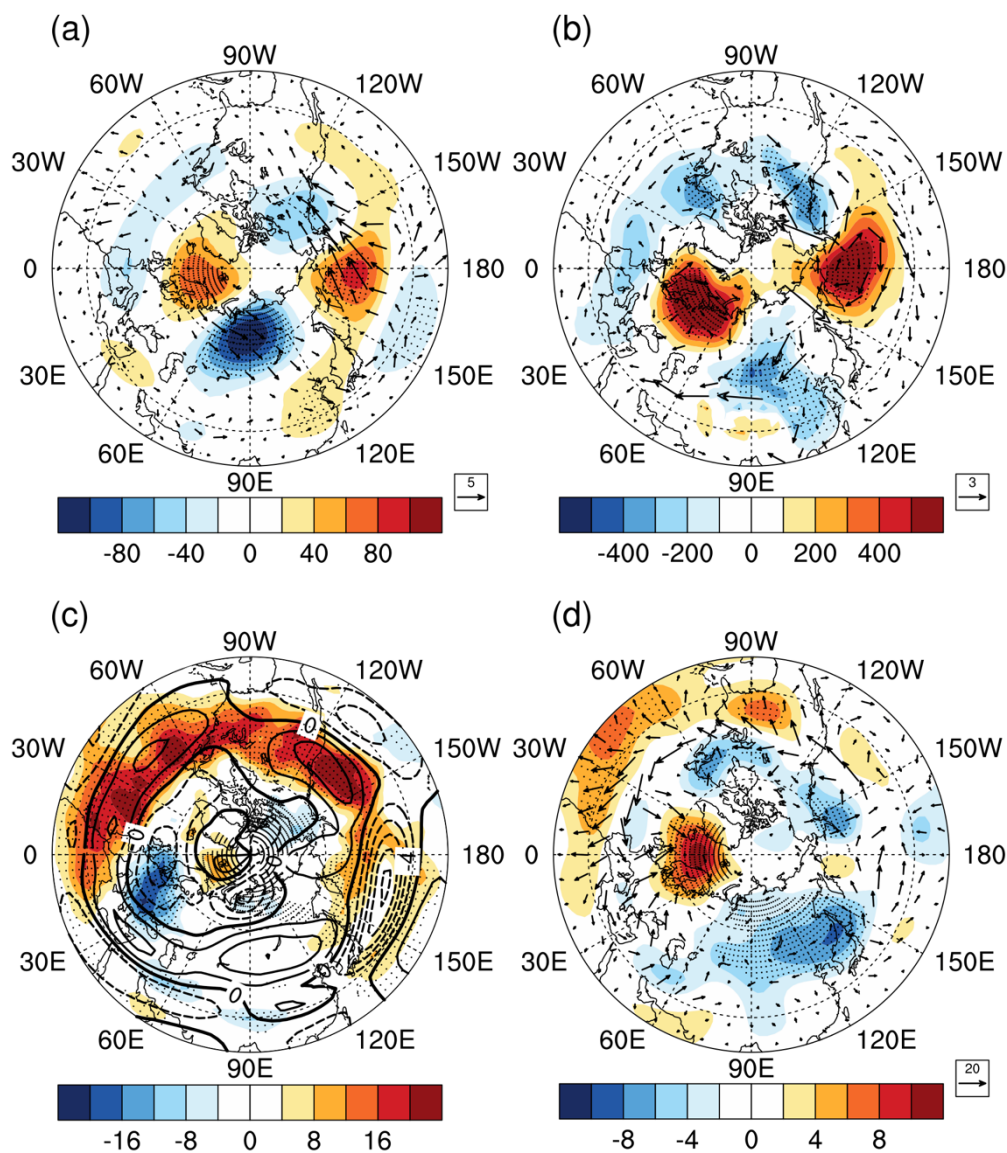
Figure 4. Winter atmospheric responses to the autumn and early winter sea ice change in the Pacific sector of the Arctic in WACCM SENSr2 extreme members with respect to the CTRL ensemble mean. (a) geopotential height (color shading, m) and wave activity flux (vectors, m² s⁻²) anomalies at 250 hPa; (b) sea level pressure (color shading, Pa) and surface wind circulation (vectors, m s⁻¹) anomalies; (c) Anomalous transient eddy kinetic energy (color shading, m² s⁻²) and zonal wind (contours, m s⁻¹) anomalies at 250 hPa; (d) Anomalous E vectors (vectors, m² s⁻²) and transient eddy-induced geopotential height tendencies (Z_t^{V+H}) (color shading, m day⁻¹) at 250 hPa. The black dots denote the 0.05 significance level.
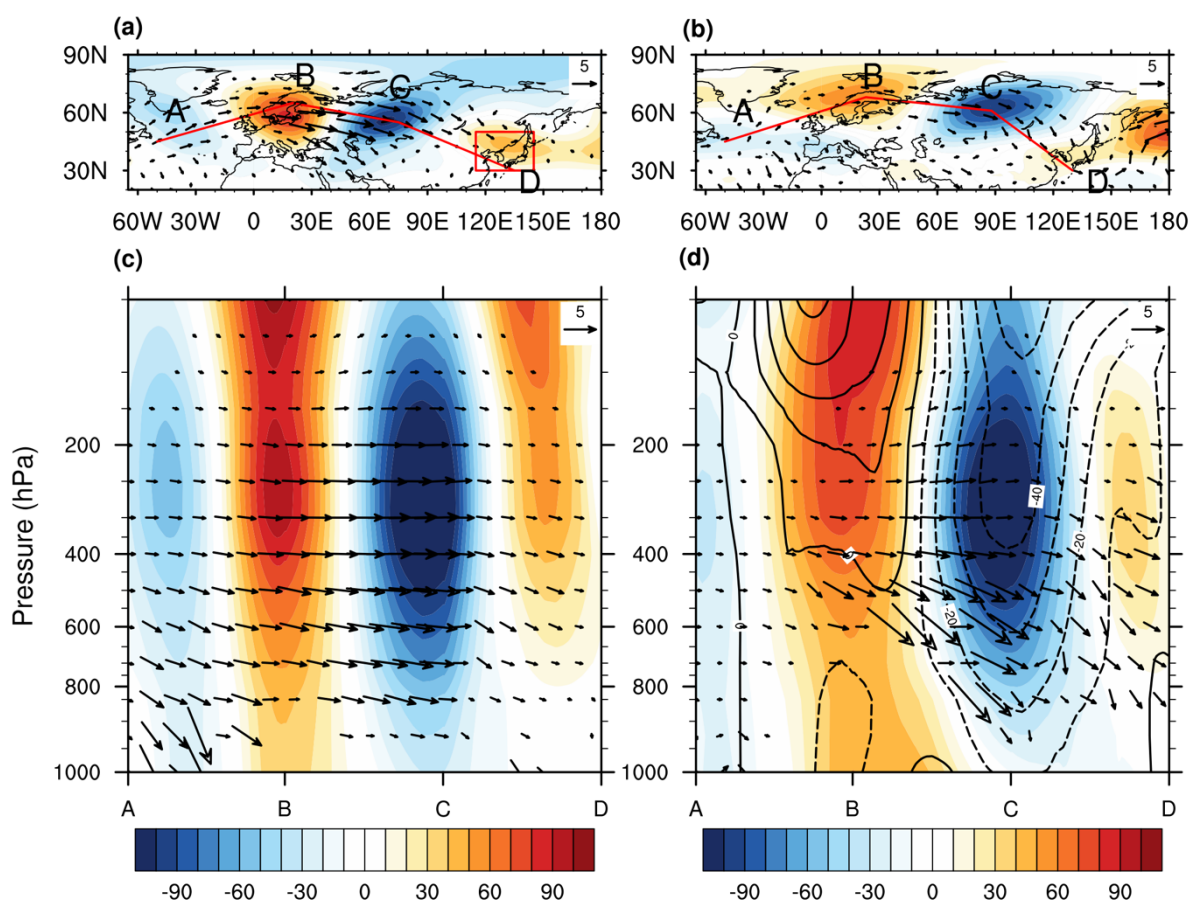
Figure 5. Comparison of the EU pattern in the NCEP reanalysis data and WACCM SENSr2 extreme members. (a) ensemble mean geopotential heights at 500 hPa (color shading, m) and wave activity flux (WAF) at 250 hPa (vectors, m² s⁻²) of the 30 strongest negative EU months in winter (DJF) of 1951-2019; (b) same as (a) but based on the differences between the SENSr2 extreme members and CTRL ensemble mean; (c) vertical cross section of geopotential heights (color shading, m) and WAF (vectors, m² s⁻²) of the ensemble mean negative EU months along the wave propagation path shown in (a); (d) same as (c) but based on the differences between the SENSr2 extreme members and CTRL ensemble mean. The contours in (d) denote the geopotential height anomaly in the counterpart CTRL members of these SENSr2 extreme members. Note that the vertical components of WAF in (c)-(d) were scaled up by 200 for clear illustration.
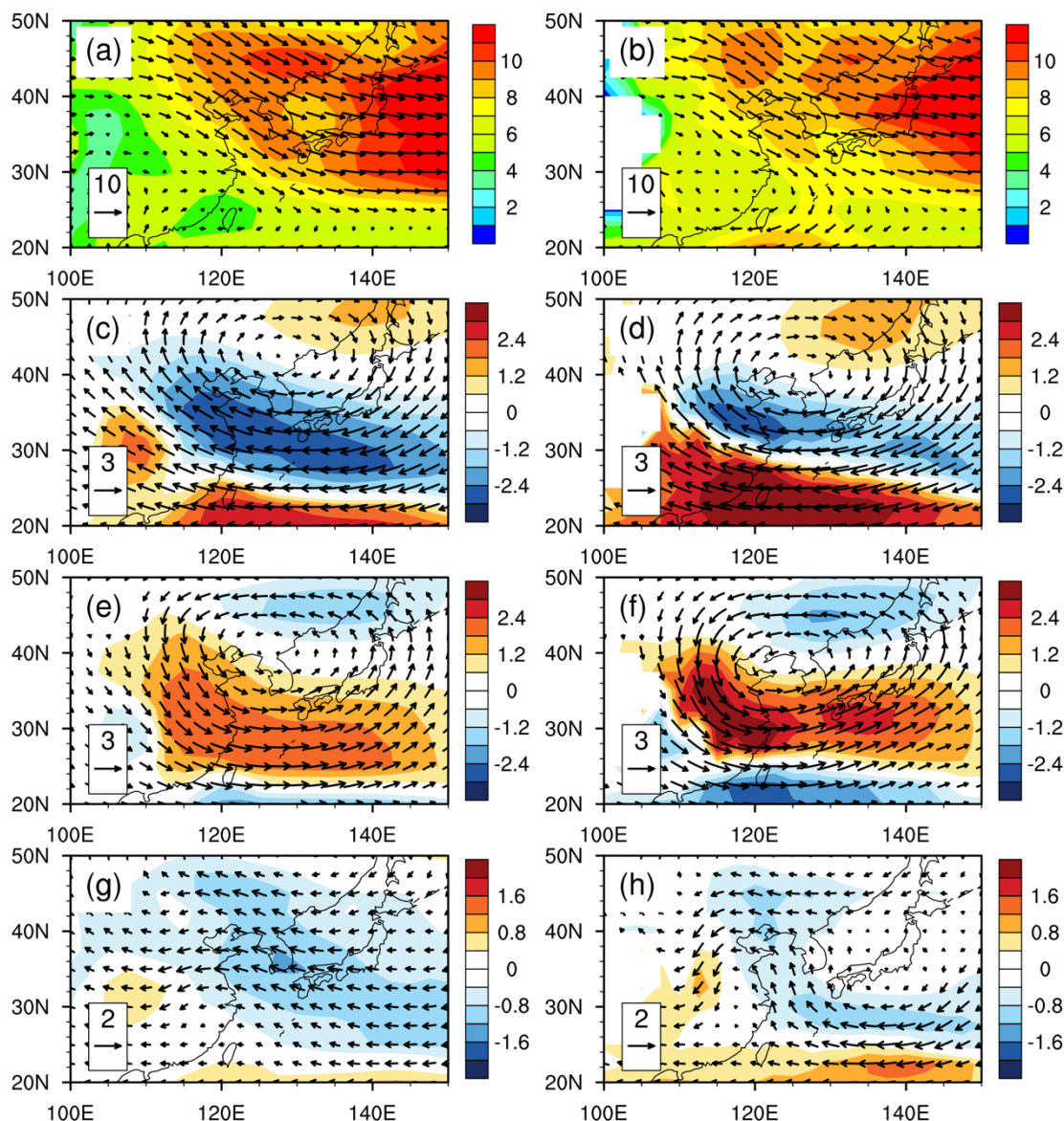
Figure 6. Comparison of winter circulation in East Asia based on the piecewise PV inversion analysis with the NCEP reanalysis and WACCM experiments. (a) climatological wind speed (color shading, m) and directions (vector, m) at 850 hPa based on the reanalysis data; (b) same as (a) but based on the WACCM CTRL ensemble mean; (c) reanalysis-based wind circulation changes at 850 hPa induced by East Asia PV anomalies (see the red box in Fig. 5a) in the middle to upper troposphere (700-100 hPa) during strong negative EU months in winter; (d) model-based wind circulation changes at 850 hPa associated with the middle to upper troposphere PV changes over East Asia between SENSr2 extreme members and CTRL ensemble mean; (e) reanalysis-based wind circulation changes at 850 hPa induced by East Asia PV anomalies in the lower troposphere (1000-850 hPa) during strong negative EU months in winter; (f) model-based wind

circulation changes at 850 hPa associated with the lower troposphere PV changes between SENSr2 extreme members and CTRL ensemble mean; (g) reanalysis-based wind circulation changes at 850 hPa induced by East Asia PV anomalies in the whole troposphere (1000-100 hPa) during strong negative EU months in winter; (h) model-based wind circulation changes at 850 hPa associated with the whole troposphere PV changes between SENSr2 extreme members and CTRL ensemble mean.
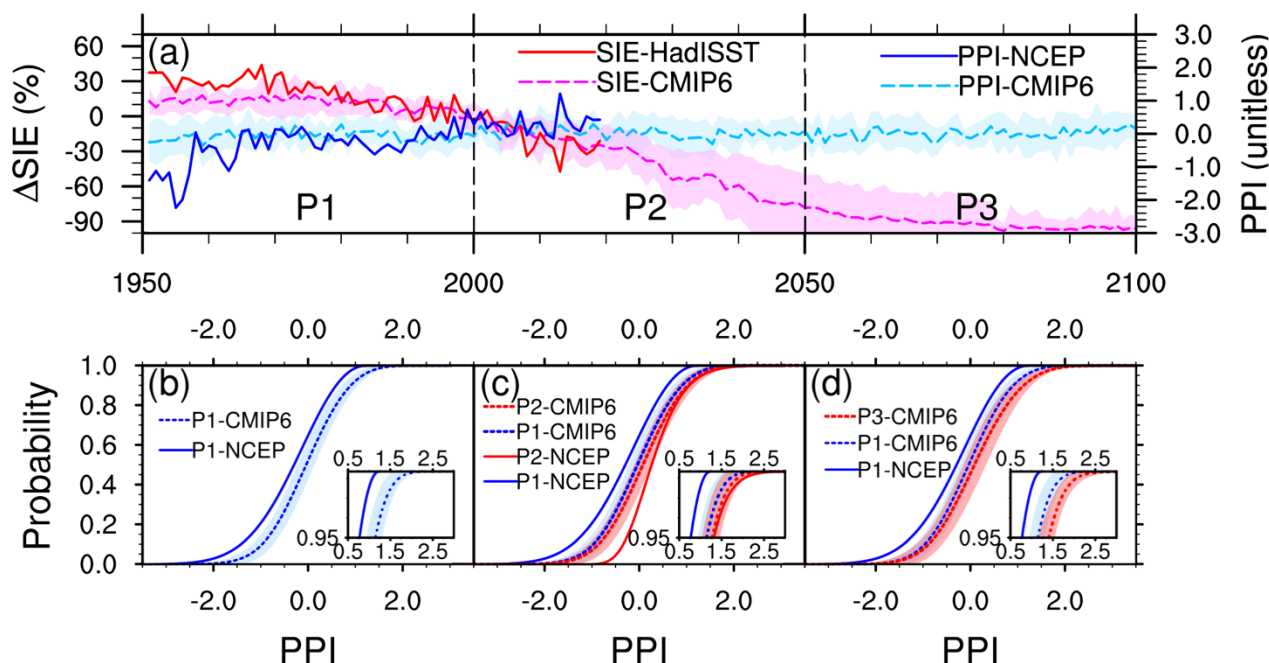
Figure 7. Historical simulations and future projections (under the SSP5-8.5 scenario) of Arctic sea ice and regional air stagnation in observational and reanalysis data and CMIP6 models. (a) time series of the Arctic SIE relative changes (unit: %; relative to 1981-2010) in preceding September and ECP_PPI (unitless) in DJF of the following winter (using years of January for X-axis labeling). The solid lines denote observation- and reanalysis-based Arctic SIE and ECP_PPI from 1950 to 2019. The dashed lines denote ensemble mean and the color shading denotes ±1 standard deviation of the 8 CMIP6 models (see Table S1 for model details) from 1950 to 2100. Note that the SIE time series were shifted one year after to be aligned with the ECP_PPI data; (b) comparison of ECP_PPI CDF curves between the NCEP reanalysis data and the CMIP6 models in the P1 time period from 1951 to 2000. The inlet denotes the distributions of positive extreme events ($\geq PPI_{P1}^{95^{th}}$). The color shading denotes ±1 standard deviations in the 8 CMIP6 models; (c) Same as (b) but for the comparison between P1 and P2 (2001-2050) time periods as well as between the NCEP reanalysis data and the CMIP6 models; (d) same as (b) but for the comparison between P1 and P3 (2051-2100) time periods as well as between the NCEP reanalysis data and the CMIP6 models. The model-specific comparison in (b)-(d) are shown in Table S5 and Fig. S7 in the Supplement.